A *QCTO-SI* Method for the Design of Enhancing Lenses for Linear Antenna Arrays

M. Salucci, G. Oliveri, N. Anselmi, G. Gottardi, and A. Massa

Abstract

In this work a novel material-by-design (*MbD*) strategy is proposed to address the problem of enhancing the radiation performance (in terms of directivity and side-lobe level) of existing linear phased arrays. Thanks to the integration of the quasi-conformal transformation optics (*QCTO*) technique with a customized source inversion (*SI*) strategy, the proposed approach enables the synthesis of meta-material lenses with reduced anisotropy indexes that are able to significantly enhance the radiation characteristics of linear antenna arrays, letting them mimic the performance of larger apertures. To prove the effectiveness of the *MbD* methodology, some numerical benchmarks are reported and discussed.

1 Half-Cosine Profile - $h' = 4.0$ [λ], $l' = 1.0$ [λ], $t' = 9.0$ [λ], $N = 15$ - Analysis vs. w'

1.1 Step 1: Expanding the physical array ($N = 15$, $L = 7.0$ [λ])

Input Parameters

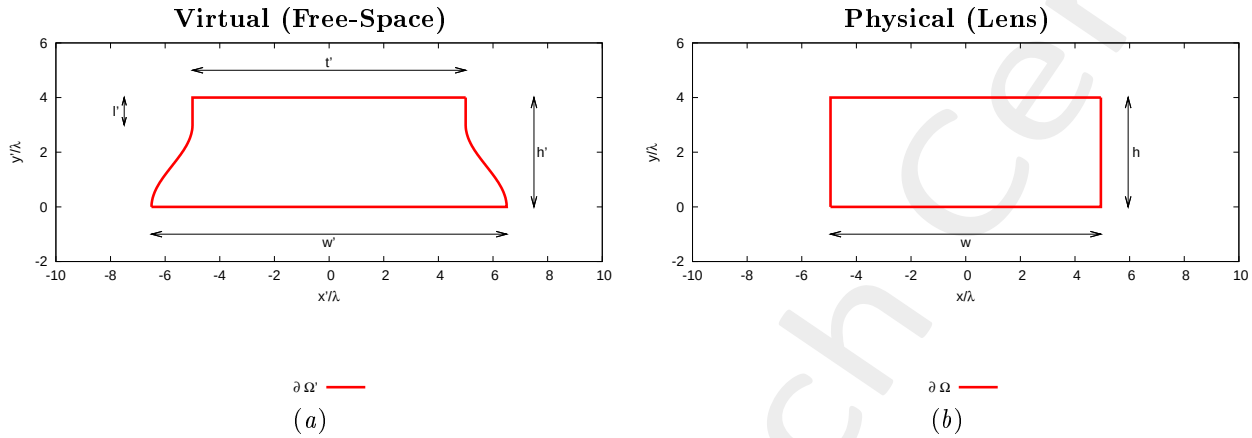

(a) (b)

Figure 1: Transformation regions. The lower side of both virtual and physical boundaries are supposed to be PEC.

- **Virtual Geometry**

# Test Case	h' [λ]	l' [λ]	t' [λ]	w' [λ]
1	4.0	1.0	9.0	**9.9**
2	4.0	1.0	9.0	**10.6**
3	4.0	1.0	9.0	**11.3**
4	4.0	1.0	9.0	**11.9**
5	4.0	1.0	9.0	**12.5**

Table I: Considered virtual geometries. The values of w' have been empirically determined in order to achieve an aperture of the virtual array (L') equal to a multiple of $\lambda/2$. It is imposed that $h = h'$, while w is not controlled by the user.

- **Physical Array**
  - Number of elements, spacing, aperture: $N = 15$, $d = \frac{\lambda}{2}$, $L = 7.0$ [λ];
  - Positions: $x_n \in [-L/2, L/2]$, $y_n = \frac{\lambda}{4}$, $n = 1, ..., N$;
  - Steering angle: $\phi_s = 90.0$ [deg];
  - Excitations: $I_n = 1.0$, $\varphi_n = \frac{-2\pi}{\lambda} x_n sin\,(\phi_s + 90)$; $n = 1, ..., N$;
- **QCTO**
  - Discretization cell dimension: 0.15 [λ] (0.01 [λ] for source mapping);

1.1.1 Results

Transformation grids

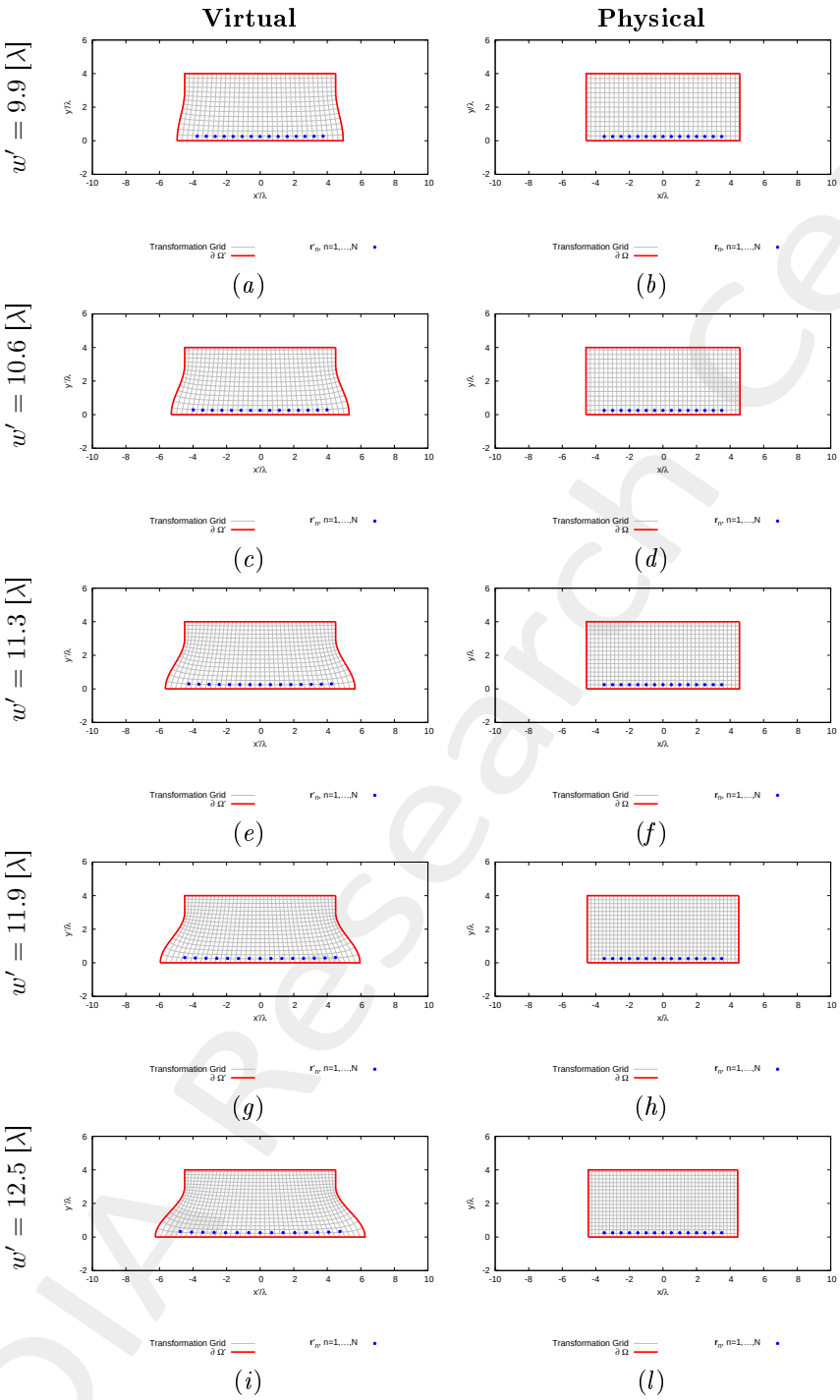

Figure 2: Transformation grids for different values of w'. Physical geometry has been shifted on y by $h/2 = 2.0$ $[\lambda]$.

Resulting aperture of the virtual array (L') - for step 2

- The aperture of the virtual array (L') is computed after mapping the physical array into the virtual space;
- The resulting number of equi-spaced elements is computed as

$$N' = round\left(\frac{L'}{0.5} + 1\right)$$

	Virtual Geometry				**Virtual Array**	
# Test Case	h' [λ]	l' [λ]	t' [λ]	w' [λ]	L' [λ]	N'
1	4.0	1.0	9.0	**9.9**	7.50	**16**
2	4.0	1.0	9.0	**10.6**	7.97	**17**
3	4.0	1.0	9.0	**11.3**	8.50	**18**
4	4.0	1.0	9.0	**11.9**	8.98	**19**
5	4.0	1.0	9.0	**12.5**	9.51	**20**

Table II: Resulting aperture and number of equi-spaced elements of the virtual array after expanding the physical array.

1.2 Step 2: Compressing the virtual array ($N' > N$, $L' > L$ [λ])

Input Parameters

- **Virtual Array**
  - Number of elements, spacing, aperture: $N' = \{16; 17; 18; 19; 20\}$, $d' = \frac{\lambda}{2}$, $L' = \{7.5; 8.0; 8.5; 9.0; 9.5\}$ $[\lambda]$;
  - Positions: $x'_n \in [-L'/2, L'/2]$, $y'_n = \lambda/4$, $n = 1, ..., N'$;
  - Steering angle: $\phi_s = 90.0$ $[deg]$;
  - Excitations: $I'_n = 1.0$, $\varphi'_n = \frac{-2\pi}{\lambda} x_n sin\,(\phi_s + 90)$; $n = 1, ..., N'$;
- **Virtual Geometry:** same of step 1;
- **QCTO:** same of step 1.

1.2.1 Results of the Transformation

Transformation grids

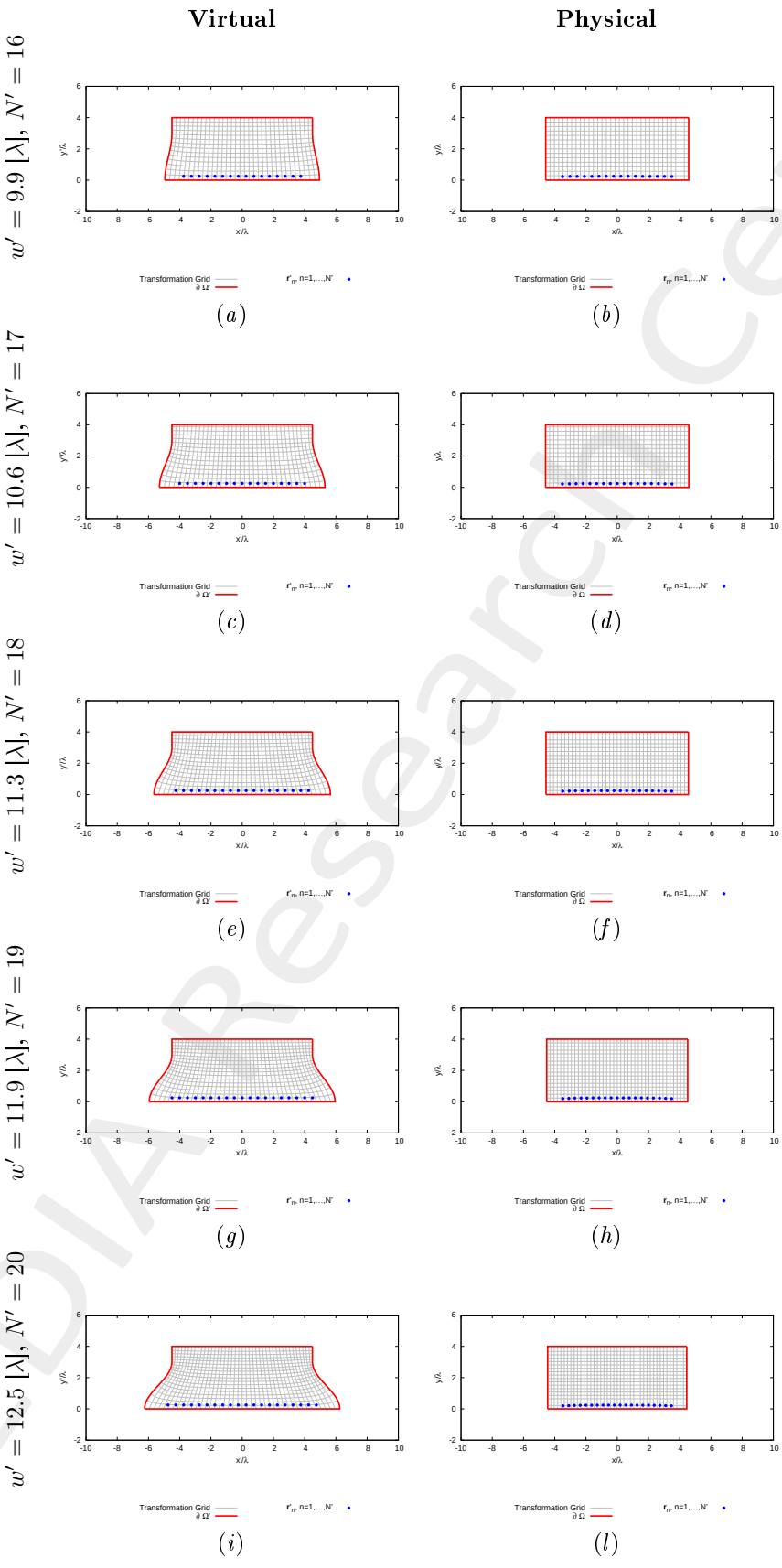

Figure 3: Transformation grids for different values of w'. Physical geometry has been shifted on y by $h/2 = 2.0$ $[\lambda]$.

Lens Permittivity - $w' = 9.9\ [\lambda]$

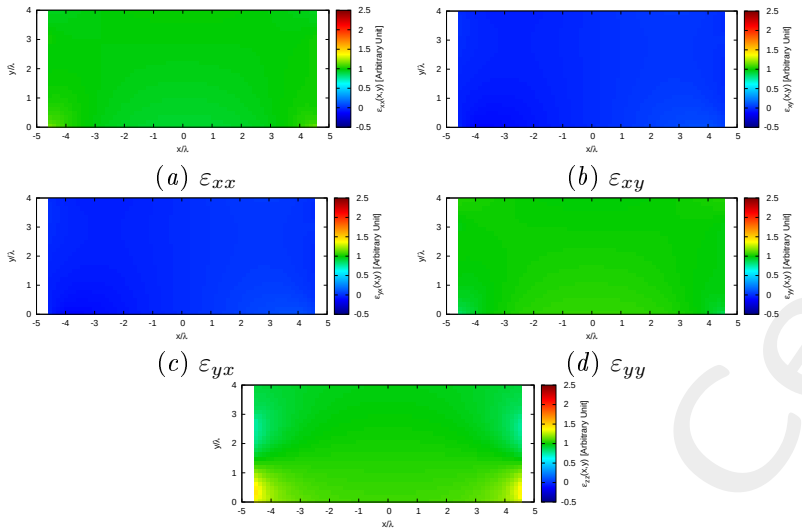

$(a)\ \varepsilon_{xx}$ $(b)\ \varepsilon_{xy}$ $(c)\ \varepsilon_{yx}$ $(d)\ \varepsilon_{yy}$ $(e)\ \varepsilon_{zz}$

Figure 4: Components of the relative permittivity tensor of the lens.

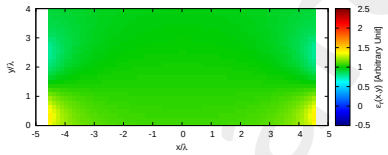

Figure 5: Isotropic approximate permittivity distribution of the lens.

Lens Permittivity - $w' = 10.6\ [\lambda]$

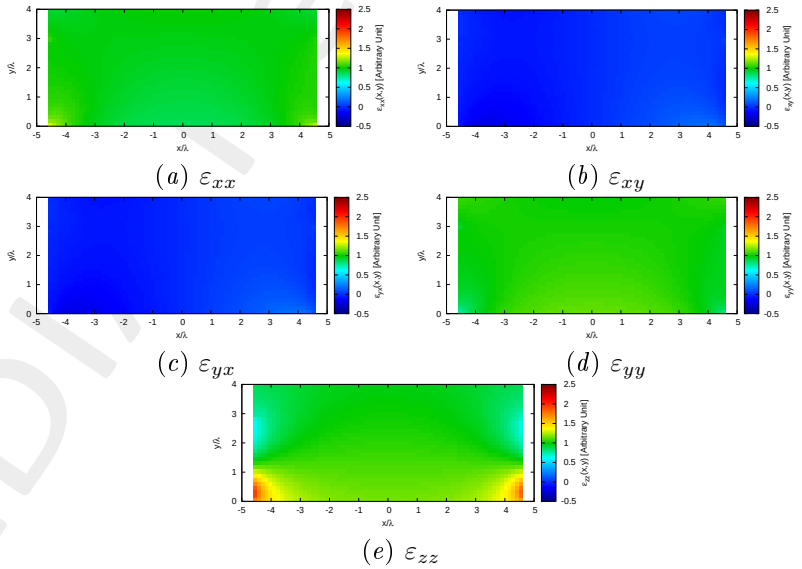

$(a)\ \varepsilon_{xx}$ $(b)\ \varepsilon_{xy}$ $(c)\ \varepsilon_{yx}$ $(d)\ \varepsilon_{yy}$ $(e)\ \varepsilon_{zz}$

Figure 6: Components of the relative permittivity tensor of the lens.

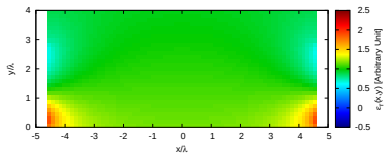

Figure 7: Isotropic approximate permittivity distribution of the lens.

Lens Permittivity - $w' = 11.3\ [\lambda]$

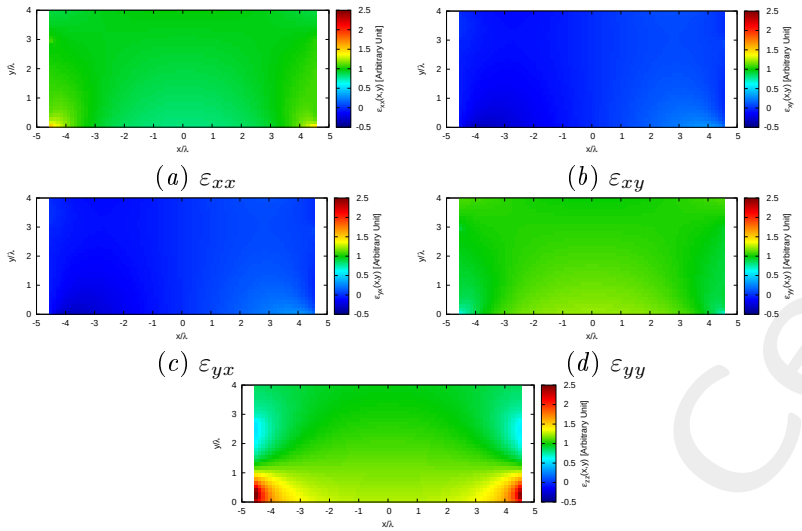

$(a)\ \varepsilon_{xx}$ $(b)\ \varepsilon_{xy}$ $(c)\ \varepsilon_{yx}$ $(d)\ \varepsilon_{yy}$ $(e)\ \varepsilon_{zz}$

Figure 8: Components of the relative permittivity tensor of the lens.

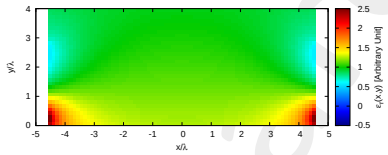

Figure 9: Isotropic approximate permittivity distribution of the lens.

Lens Permittivity - $w' = 11.9\ [\lambda]$

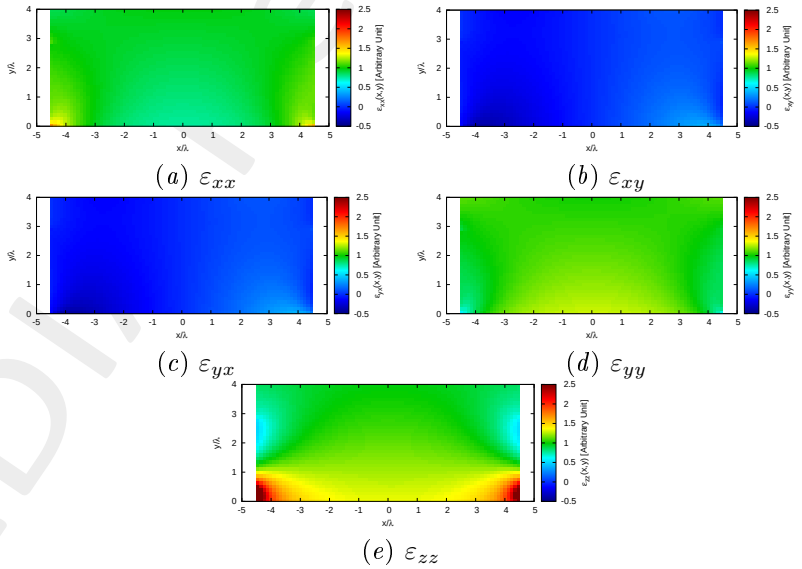

$(a)\ \varepsilon_{xx}$ $(b)\ \varepsilon_{xy}$ $(c)\ \varepsilon_{yx}$ $(d)\ \varepsilon_{yy}$ $(e)\ \varepsilon_{zz}$

Figure 10: Components of the relative permittivity tensor of the lens.

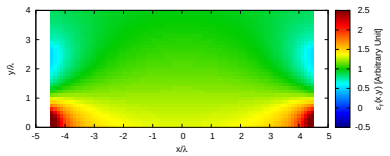

Figure 11: Isotropic approximate permittivity distribution of the lens.

Lens Permittivity - $w' = 12.5\ [\lambda]$

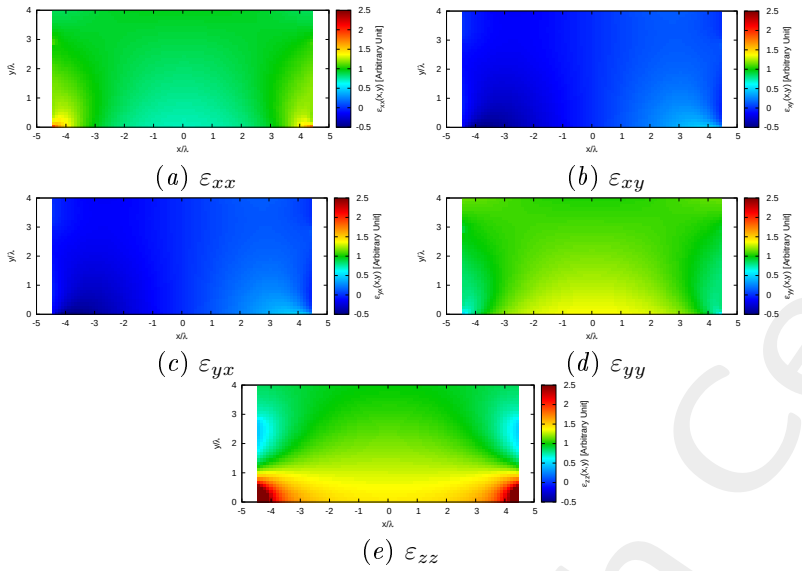

Figure 12: Components of the relative permittivity tensor of the lens.

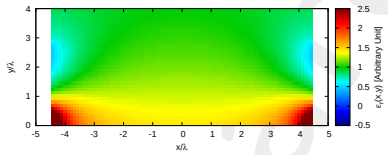

Figure 13: Isotropic approximate permittivity distribution of the lens.

Physical Lens Parameters

Parameter	$w^{'} = 9.9\ [\lambda]$	$w^{'} = 10.6\ [\lambda]$	$w^{'} = 11.3\ [\lambda]$	$w^{'} = 11.9\ [\lambda]$	$w^{'} = 12.5\ [\lambda]$
Height, $h\ [\lambda]$	4.00	4.00	4.00	4.00	4.00
Width, $w\ [\lambda]$	9.16	9.17	9.12	9.02	8.91
Anisotropic Permittivity Range	$[-0.11, 1.44]$	$[-0.20, 1.95]$	$[-0.30, 2.65]$	$[-0.39, 3.48]$	$[-0.48, 4.53]$
Isotropic Permittivity Range	$[0.00, 1.42]$	$[0.00, 1.90]$	$[0.00, 2.59]$	$[0.00, 3.37]$	$[0.00, 4.33]$
Average Fractional Anisotropy, α_F	5.66×10^{-2}	1.01×10^{-1}	1.44×10^{-1}	1.81×10^{-1}	2.15×10^{-1}
Average Relative Anisotropy, α_R	4.67×10^{-2}	8.43×10^{-2}	1.23×10^{-1}	1.57×10^{-1}	1.90×10^{-1}

Table III: Transformation statistics. Note that we impose $h = h'$, while w is internally chosen by the QCTO software.

1.2.2 Far-Field Patterns ($\phi_s = 90$ [deg], $f = 600$ [MHz])

Anisotropic Lens

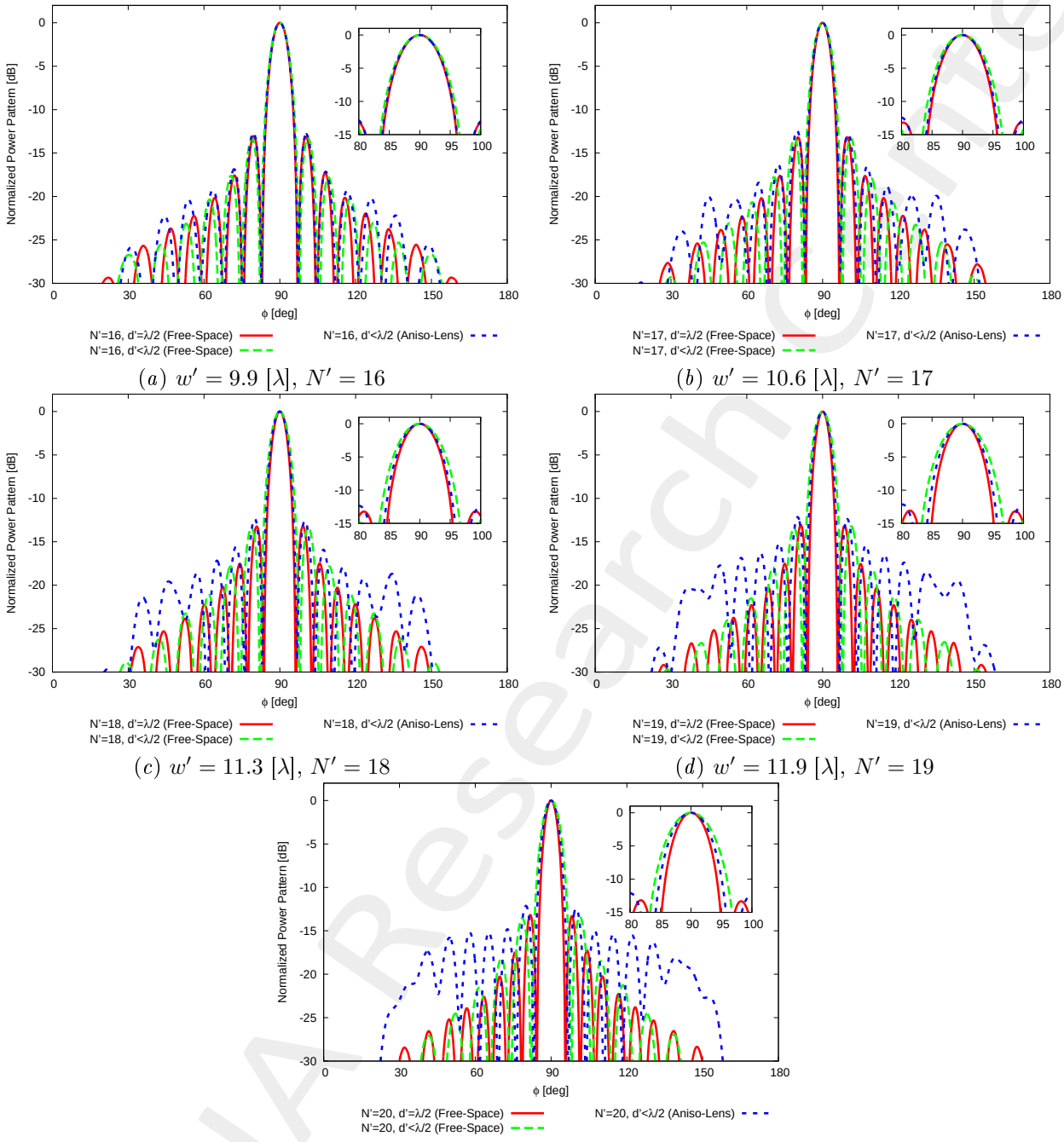

(a) $w' = 9.9$ $[\lambda]$, $N' = 16$ (b) $w' = 10.6$ $[\lambda]$, $N' = 17$

(c) $w' = 11.3$ $[\lambda]$, $N' = 18$ (d) $w' = 11.9$ $[\lambda]$, $N' = 19$

(e) $w' = 12.5$ $[\lambda]$, $N' = 20$

Figure 14: Far field pattern comparison for different values of w'.

Isotropic Lens

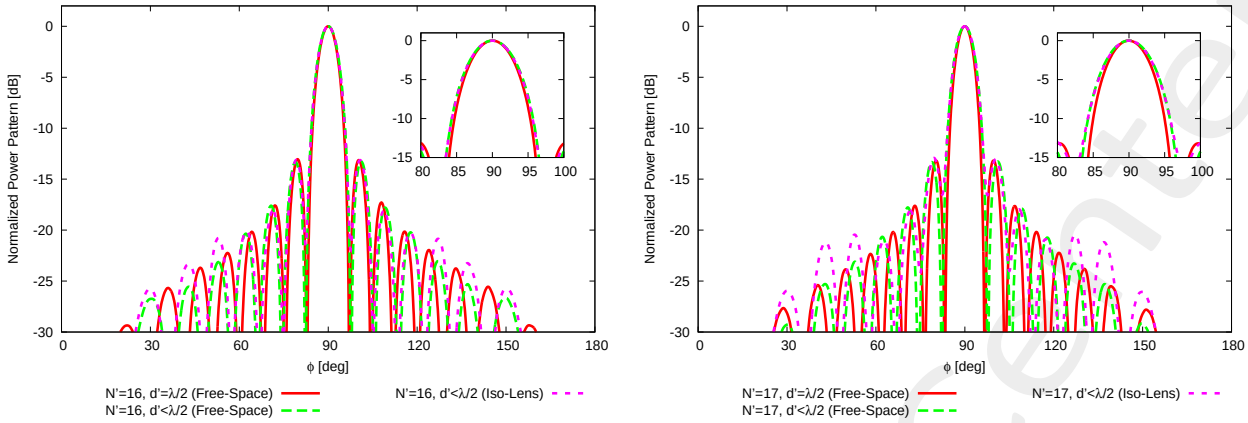

(a) $w' = 9.9$ $[\lambda]$, $N' = 16$

(b) $w' = 10.6$ $[\lambda]$, $N' = 17$

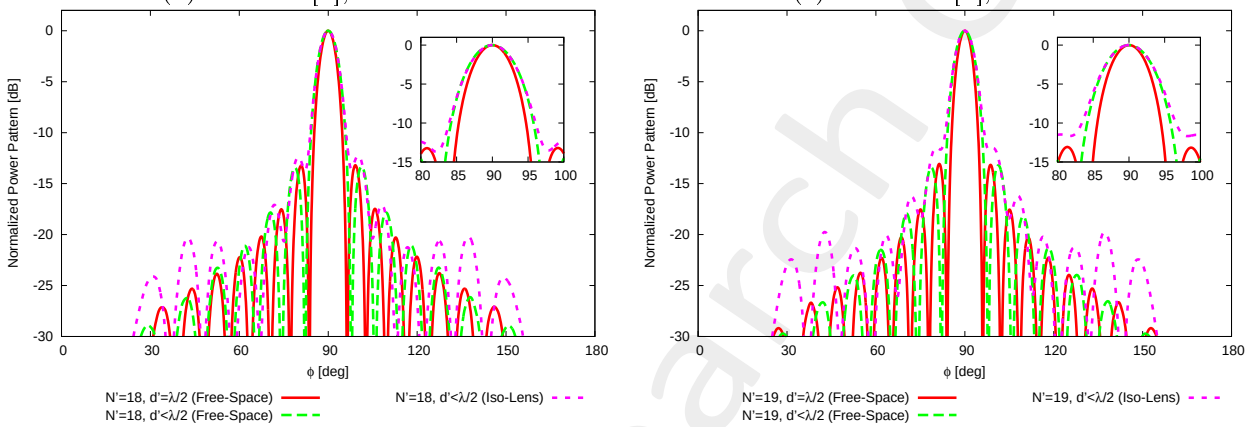

(c) $w' = 11.3$ $[\lambda]$, $N' = 18$

(d) $w' = 11.9$ $[\lambda]$, $N' = 19$

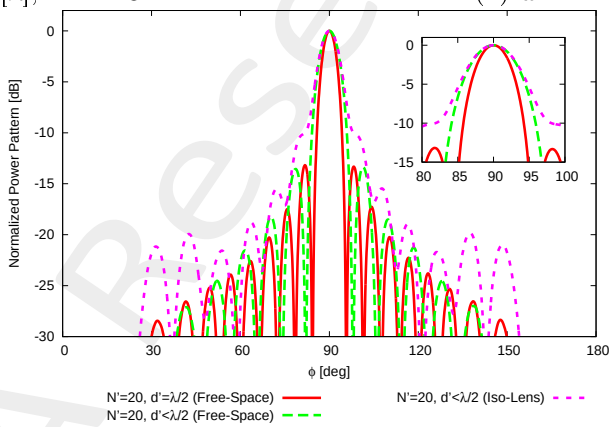

(e) $w' = 12.5$ $[\lambda]$, $N' = 20$

Figure 15: Far field pattern comparison for different values of w'.

1.2.3 Summary ($\phi_s = 90$ [deg], $f = 600$ [MHz])

$w' = 9.9$ [λ]				
	Virtual Array	**Physical Array**		
Environment	Free-Space	Free-Space	Aniso-Lens	Iso-Lens
Number of elements	16	16		
Spacing [λ]	0.5	< 0.5		
Aperture [λ]	7.5	6.99		
$D_{\max}$ [dB]	13.97	13.72	13.82	13.70
SLL [dB]	13.11	13.26	12.66	13.11
$FNBW$ [deg]	14.32	15.40	14.50	15.22
3dB Beamwidth [deg]	6.36	6.80	6.46	6.71
Matching Error, ξ (w.r.t. virtual, outside lens)	-	3.50×10^{-1}	3.74×10^{-1}	5.77×10^{-1}

$w' = 10.6$ [λ]				
	Virtual Array	**Physical Array**		
Environment	Free-Space	Free-Space	Aniso-Lens	Iso-Lens
Number of elements	17	17		
Spacing [λ]	0.5	< 0.5		
Aperture [λ]	8.0	7.01		
$D_{\max}$ [dB]	14.25	13.71	13.88	13.60
SLL [dB]	13.16	13.27	12.41	12.92
$FNBW$ [deg]	13.60	15.58	13.96	15.22
3dB Beamwidth [deg]	5.97	6.83	6.23	6.72
Matching Error, ξ (w.r.t. virtual, outside lens)	-	5.82×10^{-1}	5.41×10^{-1}	9.06×10^{-1}

$w' = 11.3$ [λ]				
	Virtual Array	**Physical Array**		
Environment	Free-Space	Free-Space	Aniso-Lens	Iso-Lens
Number of elements	18	18		
Spacing [λ]	0.5	< 0.5		
Aperture [λ]	8.5	6.97		
$D_{\max}$ [dB]	14.50	13.68	13.86	13.38
SLL [dB]	13.14	13.33	12.37	12.27
$FNBW$ [deg]	12.79	15.76	13.69	15.58
3dB Beamwidth [deg]	5.64	6.90	6.10	6.84
Matching Error, ξ (w.r.t. virtual, outside lens)	-	6.99×10^{-1}	5.54×10^{-1}	1.13

$w' = 11.9$ [λ]				
	Virtual Array	**Physical Array**		
Environment	Free-Space	Free-Space	Aniso-Lens	Iso-Lens
Number of elements	19	19		
Spacing [λ]	0.5	< 0.5		
Aperture [λ]	9.0	6.96		
$D_{\max}$ [dB]	14.73	13.65	13.76	13.09
SLL [dB]	13.06	13.21	12.16	11.47
$FNBW$ [deg]	12.07	15.76	13.51	16.48
3dB Beamwidth [deg]	5.35	6.97	6.04	7.07
Matching Error, ξ (w.r.t. virtual, outside lens)	-	6.89×10^{-1}	6.41×10^{-1}	1.34

$w' = 12.5$ [λ]				
	Virtual Array	**Physical Array**		
Environment	Free-Space	Free-Space	Aniso-Lens	Iso-Lens
Number of elements	20	20		
Spacing [λ]	0.5	< 0.5		
Aperture [λ]	9.5	6.94		
$D_{\max}$ [dB]	14.96	13.63	13.53	12.73
SLL [dB]	13.18	13.38	12.12	15.46
$FNBW$ [deg]	11.44	15.94	13.60	29.99
3dB Beamwidth [deg]	5.06	7.04	6.08	7.38
Matching Error, ξ (w.r.t. virtual, outside lens)	-	7.18×10^{-1}	8.04×10^{-1}	1.51

Table IV: Summary for step 2.

1.3 Source Inversion (SI)

Parameters

- Before SI
  - Number of elements: $N' = \{16; 17; 18; 19; 20\}$, $d' < \lambda/2$;
- After SI
  - Number of elements after SI: $N = 15$, $d = \frac{\lambda}{2}$;
  - Aperture: $L = 7.0$;
- Radius of the observation domain: $r_{SI} = 50.0$ [λ];
- Number of field sampling points: $n_{SI} = 1000$.

1.3.1 Far-Field Patterns ($\phi_s = 90$ [deg], $f = 600$ [MHz])

Anisotropic Lens

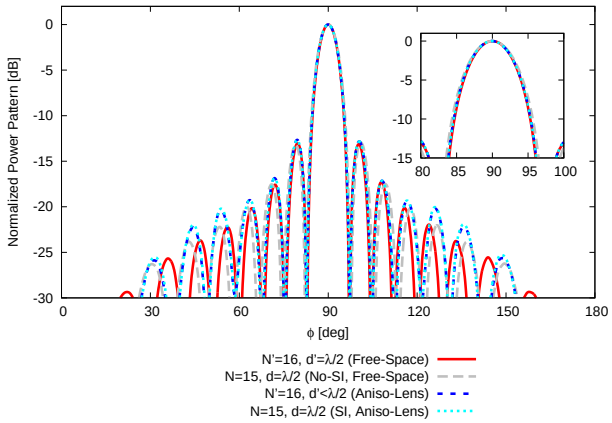

(a) $w' = 9.9$ $[\lambda]$, $N' = 16$

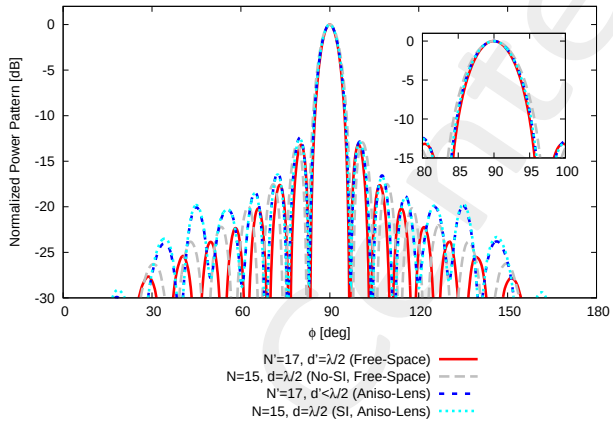

(b) $w' = 10.6$ $[\lambda]$, $N' = 17$

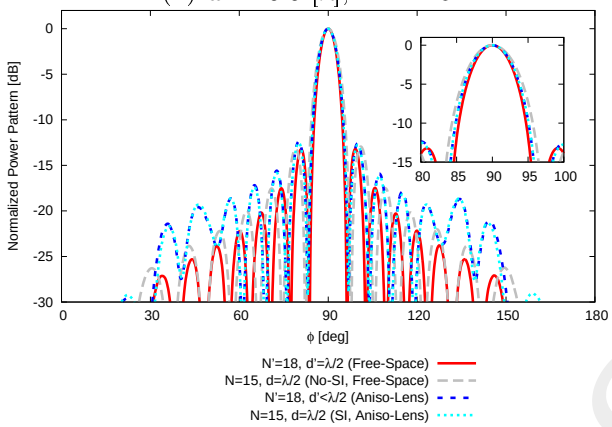

(c) $w' = 11.3$ $[\lambda]$, $N' = 18$

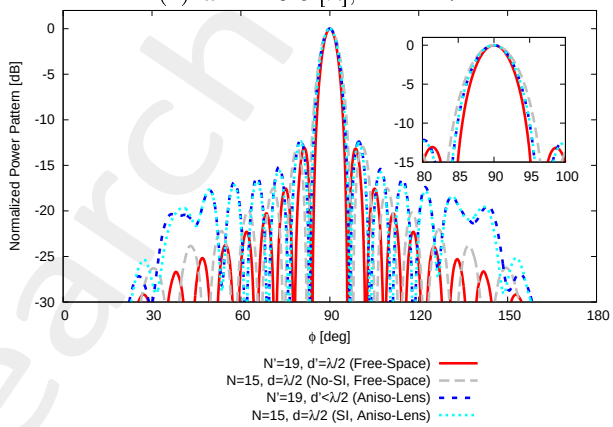

(d) $w' = 11.9$ $[\lambda]$, $N' = 19$

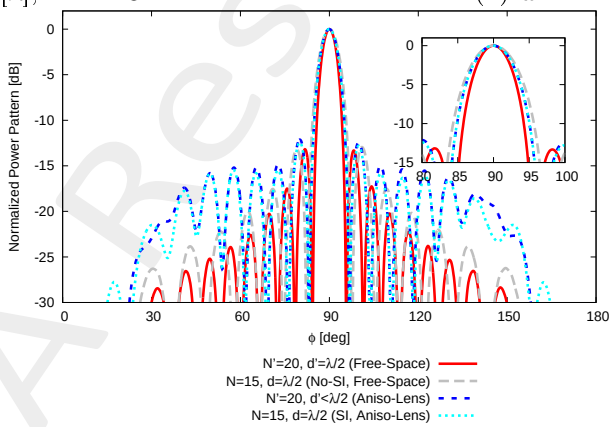

(e) $w' = 12.5$ $[\lambda]$, $N' = 20$

Figure 16: $\phi_s = 90$ [deg], $f = 600$ [MHz] - Far field pattern comparison for different values of w'.

Isotropic Lens

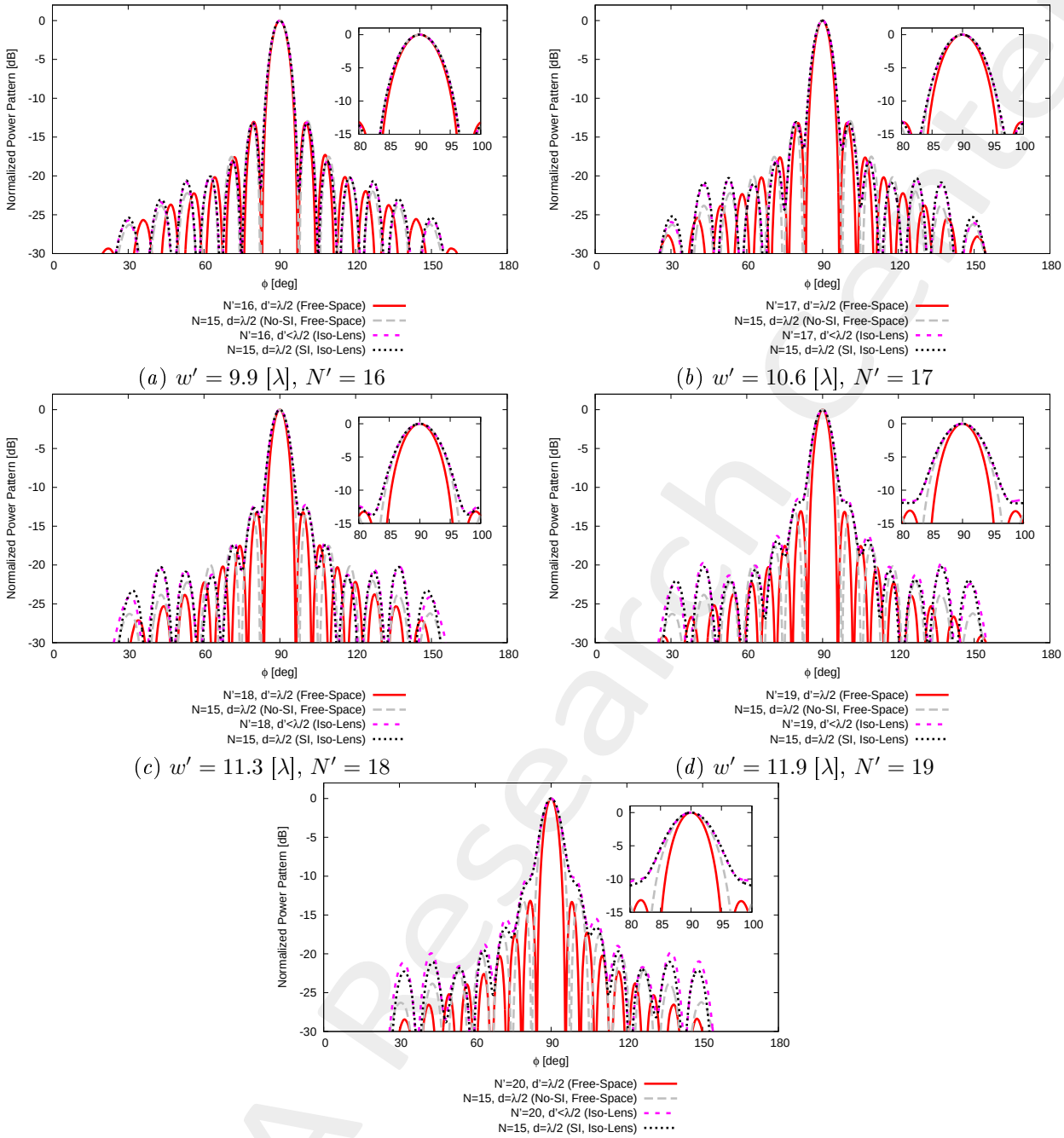

(a) $w' = 9.9$ $[\lambda]$, $N' = 16$

(b) $w' = 10.6$ $[\lambda]$, $N' = 17$

(c) $w' = 11.3$ $[\lambda]$, $N' = 18$

(d) $w' = 11.9$ $[\lambda]$, $N' = 19$

(e) $w' = 12.5$ $[\lambda]$, $N' = 20$

Figure 17: $\phi_s = 90$ [deg], $f = 600$ [MHz] - Far field pattern comparison for different values of w'.

1.3.2 Final Summary ($\phi_s = 90$ [deg], $f = 600$ [MHz])

$w' = 9.9$ [λ]				
	Virtual Array	**Physical Array**		
Environment	Free-Space	Free-Space (No-SI)	Aniso-Lens (SI)	Iso-Lens (SI)
Number of elements	16	15		
Spacing [λ]	0.5	0.5		
Aperture [λ]	7.5	7.0		
$D_{\max}$ [dB]	13.97	13.71	13.81	13.69
SLL [dB]	13.11	13.08	12.67	13.15
$FNBW$ [deg]	14.32	15.31	14.50	15.22
3dB Beamwidth [deg]	6.36	6.76	6.46	6.72
Matching Error, ξ (w.r.t. virtual, outside lens)	-	3.24×10^{-1}	3.75×10^{-1}	5.76×10^{-1}
$w' = 10.6$ [λ]				
	Virtual Array	**Physical Array**		
Environment	Free-Space	Free-Space (No-SI)	Aniso-Lens (SI)	Iso-Lens (SI)
Number of elements	17	15		
Spacing [λ]	0.5	0.5		
Aperture [λ]	8.0	7.0		
$D_{\max}$ [dB]	14.25	13.71	13.88	13.59
SLL [dB]	13.16	13.08	12.53	13.07
$FNBW$ [deg]	13.60	15.31	14.05	15.40
3dB Beamwidth [deg]	5.97	6.76	6.24	6.74
Matching Error, ξ (w.r.t. virtual, outside lens)	-	5.57×10^{-1}	5.47×10^{-1}	9.13×10^{-1}
$w' = 11.3$ [λ]				
	Virtual Array	**Physical Array**		
Environment	Free-Space	Free-Space (No-SI)	Aniso-Lens (SI)	Iso-Lens (SI)
Number of elements	18	15		
Spacing [λ]	0.5	0.5		
Aperture [λ]	8.5	7.0		
$D_{\max}$ [dB]	14.50	13.71	13.87	13.38
SLL [dB]	13.14	13.08	12.52	12.53
$FNBW$ [deg]	12.79	15.31	13.78	15.94
3dB Beamwidth [deg]	5.64	6.76	6.12	6.88
Matching Error, ξ (w.r.t. virtual, outside lens)	-	6.60×10^{-1}	5.63×10^{-1}	1.09
$w' = 11.9$ [λ]				
	Virtual Array	**Physical Array**		
Environment	Free-Space	Free-Space (No-SI)	Aniso-Lens (SI)	Iso-Lens (SI)
Number of elements	19	15		
Spacing [λ]	0.5	0.5		
Aperture [λ]	9.0	7.0		
$D_{\max}$ [dB]	14.73	13.71	13.78	13.11
SLL [dB]	13.06	13.08	12.34	11.89
$FNBW$ [deg]	12.07	15.31	13.69	17.02
3dB Beamwidth [deg]	5.35	6.76	6.07	7.16
Matching Error, ξ (w.r.t. virtual, outside lens)	-	6.46×10^{-1}	6.15×10^{-1}	1.29
$w' = 12.5$ [λ]				
	Virtual Array	**Physical Array**		
Environment	Free-Space	Free-Space (No-SI)	Aniso-Lens (SI)	Iso-Lens (SI)
Number of elements	20	15		
Spacing [λ]	0.5	0.5		
Aperture [λ]	9.5	7.0		
$D_{\max}$ [dB]	14.96	13.71	13.63	12.80
SLL [dB]	13.18	13.08	12.42	16.60
$FNBW$ [deg]	11.44	15.31	13.69	30.70
3dB Beamwidth [deg]	5.06	6.76	6.09	7.50
Matching Error, ξ (w.r.t. virtual, outside lens)	-	6.46×10^{-1}	7.67×10^{-1}	1.47

Table V: $\phi_s = 90$ [deg], $f = 600$ [MHz] - Final summary.

1.3.3 Final Summary: Performances vs. w' (vs. N')

Anisotropic Lens - $\phi_s = 90$ [deg]

This figure compares the pattern characteristics of

1. Original array ($N = 15$ elements, $d = \lambda/2$, Free-Space) - GREY;
2. Target array ($N' > N$ elements, $d = \lambda/2$, Free-Space) - RED;
3. QCTO-SI array ($N = 15$ elements, $d = \lambda/2$, Anisotropic Lens + SI) - CYAN;

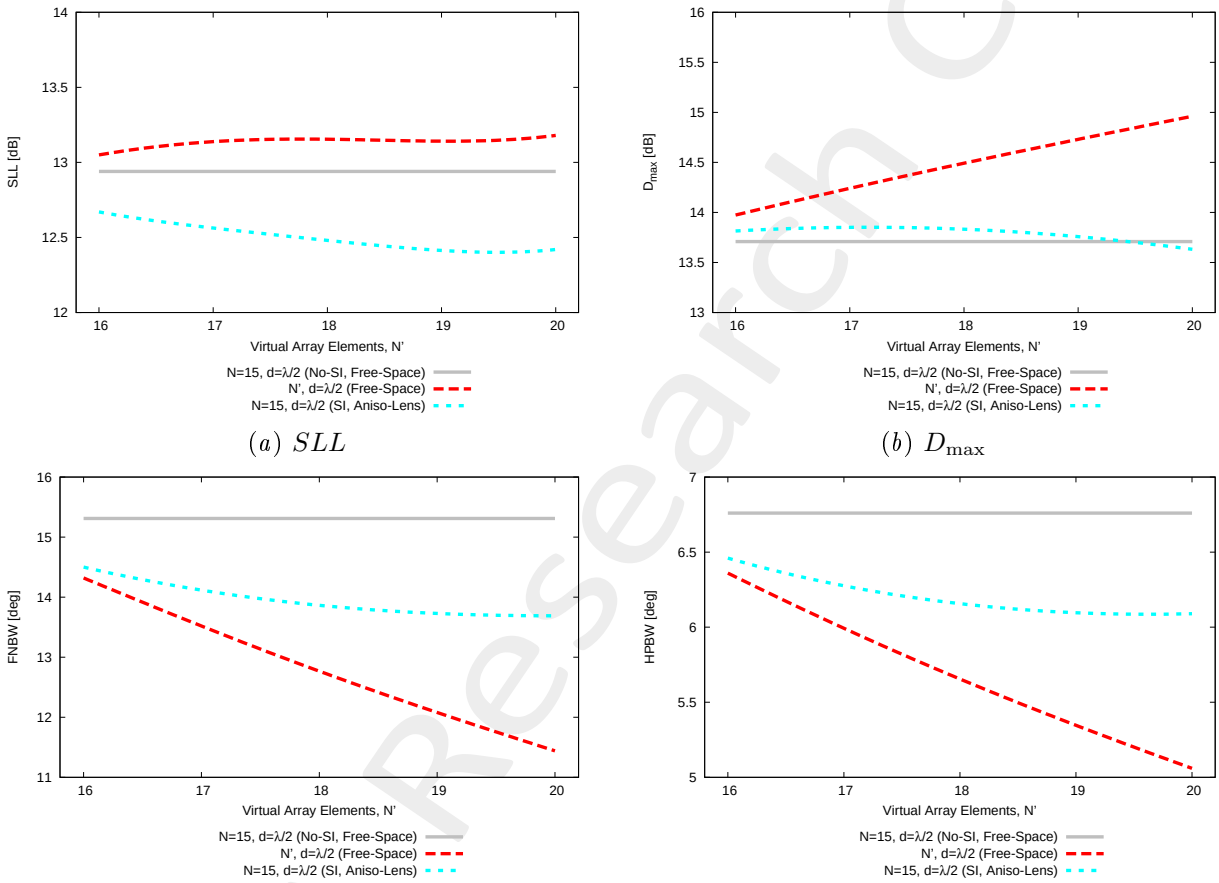

(a) SLL (b) $D_{\max}$

(b) $FNBW$ (c) $HPBW$

Figure 18: Aniso-Lens, $f = 600$ [MHz] - Pattern performances vs w' (vs. N').

2 Half-Cosine Profile - $h' = 4.0$ [λ], $l' = 0.0$ [λ], $t' = 9.0$ [λ], $N = 15$ - Analysis vs. w'

What Changed?

With respect to the previous test case, here we change the value of $l^{'}$

$$l^{'} = 1.0[\lambda] \rightarrow 0.0[\lambda]$$

all other parameters (i.e., $h^{'}$, $l^{'}$, N) are kept.

NOTE: The values of w' must be however re-determined for this new configuration.

2.1 Step 1: Expanding the physical array ($N = 15$, $L = 7.0$ [λ])

Input Parameters

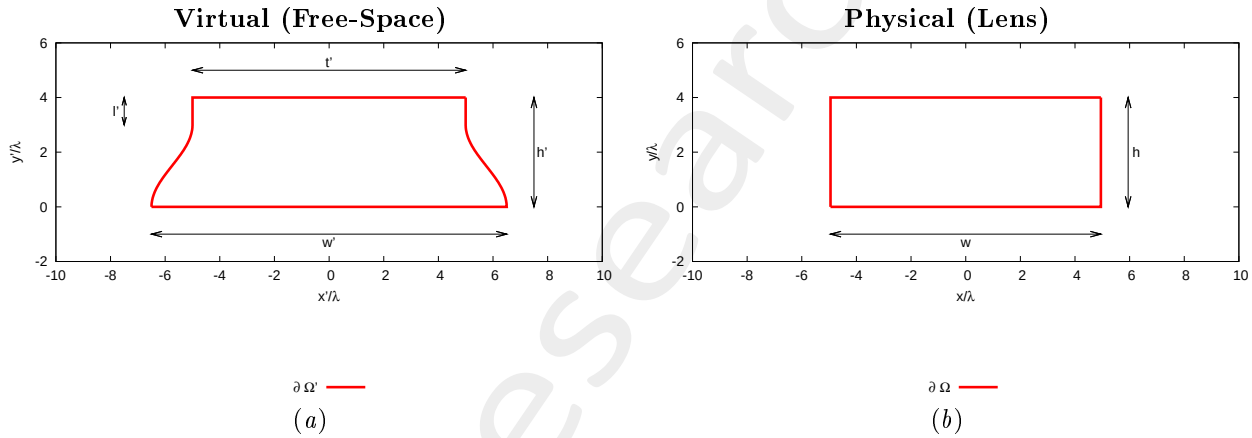

Figure 19: Transformation regions. The lower side of both virtual and physical boundaries are supposed to be PEC.

- **Virtual Geometry**

# Test Case	h' [λ]	l' [λ]	t' [λ]	w' [λ]
1	4.0	0.0	9.0	**10.3**
2	4.0	0.0	9.0	**11.3**
3	4.0	0.0	9.0	**12.1**
4	4.0	0.0	9.0	**12.9**
5	4.0	0.0	9.0	**13.6**

Table VI: Considered virtual geometries. The values of w' have been empirically determined in order to achieve an aperture of the virtual array (L') equal to a multiple of $\lambda/2$. It is imposed that $h = h'$, while w is not controlled by the user.

- **Physical Array**
  - Number of elements, spacing, aperture: $N = 15$, $d = \frac{\lambda}{2}$, $L = 7.0$ [λ];
  - Positions: $x_n \in [-L/2, L/2]$, $y_n = \frac{\lambda}{4}$, $n = 1, ..., N$;

- Steering angle: $\phi_s = 90.0$ $[deg]$;
- Excitations: $I_n = 1.0$, $\varphi_n = \frac{-2\pi}{\lambda} x_n sin\,(\phi_s + 90)$; $n = 1, ..., N$;

- **QCTO**
  - Discretization cell dimension: 0.15 $[\lambda]$ (0.01 $[\lambda]$ for source mapping);

2.1.1 Results

Transformation grids

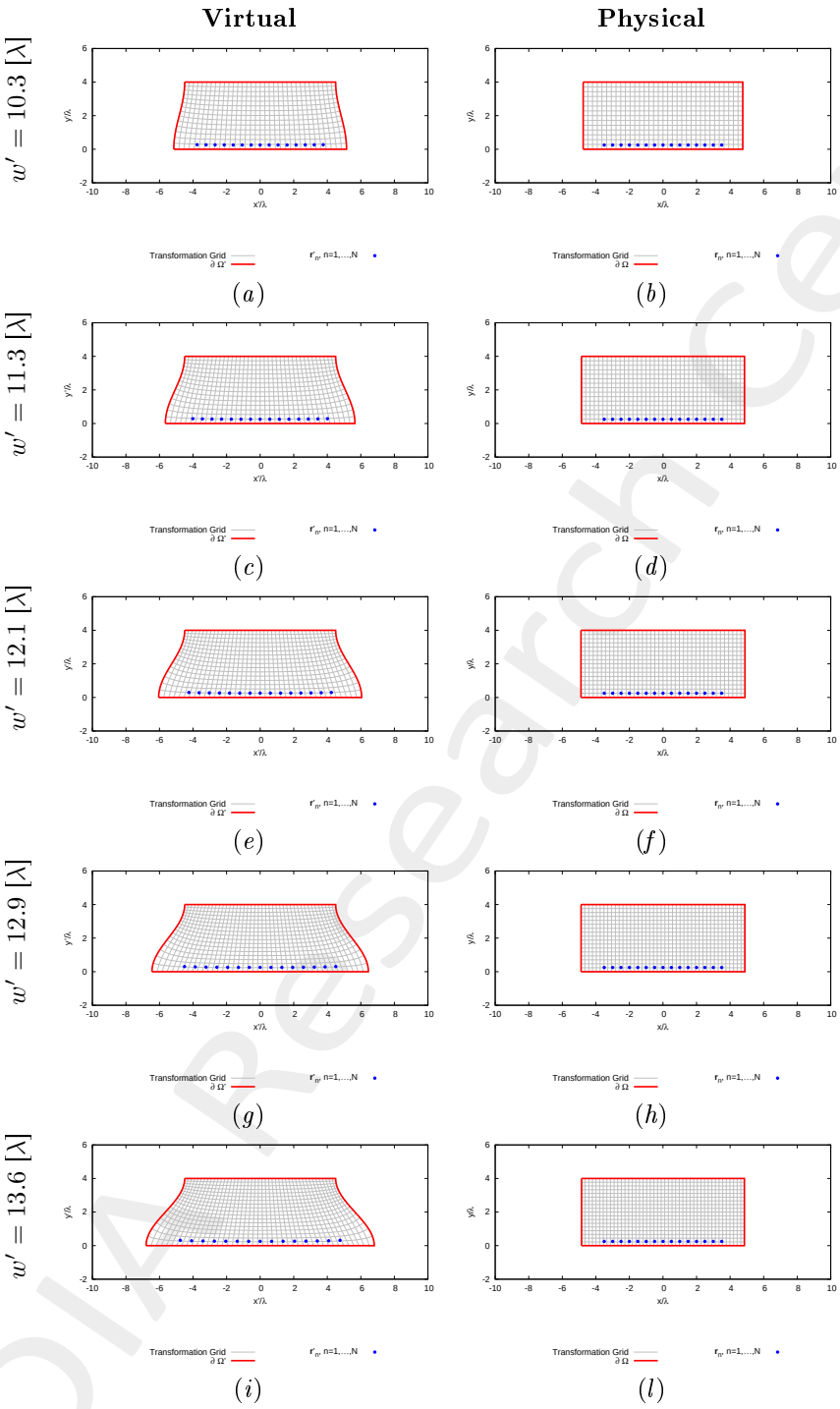

Figure 20: Transformation grids for different values of w'. Physical geometry has been shifted on y by $h/2 = 2.0$ $[\lambda]$.

Resulting aperture of the virtual array (L') - for step 2

- The aperture of the virtual array (L') is computed after mapping the physical array into the virtual space;
- The resulting number of equi-spaced elements is computed as

$$N' = round\left(\frac{L'}{0.5} + 1\right)$$

	Virtual Geometry				**Virtual Array**	
# Test Case	h' [λ]	l' [λ]	t' [λ]	w' [λ]	L' [λ]	N'
1	4.0	0.0	9.0	**10.3**	7.52	**16**
2	4.0	0.0	9.0	**11.3**	8.02	**17**
3	4.0	0.0	9.0	**12.1**	8.49	**18**
4	4.0	0.0	9.0	**12.9**	9.01	**19**
5	4.0	0.0	9.0	**13.6**	9.52	**20**

Table VII: Resulting aperture and number of equi-spaced elements of the virtual array after expanding the physical array.

2.2 Step 2: Compressing the virtual array ($N' > N$, $L' > L$ [λ])

Input Parameters

- **Virtual Array**
  - Number of elements, spacing, aperture: $N' = \{16; 17; 18; 19; 20\}$, $d' = \frac{\lambda}{2}$, $L' = \{7.5; 8.0; 8.5; 9.0; 9.5\}$ $[\lambda]$;
  - Positions: $x'_n \in [-L'/2, L'/2]$, $y'_n = \lambda/4$, $n = 1, ..., N'$;
  - Steering angle: $\phi_s = 90.0$ $[deg]$;
  - Excitations: $I'_n = 1.0$, $\varphi'_n = \frac{-2\pi}{\lambda} x_n sin\,(\phi_s + 90)$; $n = 1, ..., N'$;
- **Virtual Geometry:** same of step 1;
- **QCTO:** same of step 1.

2.2.1 Results of the Transformation

Transformation grids

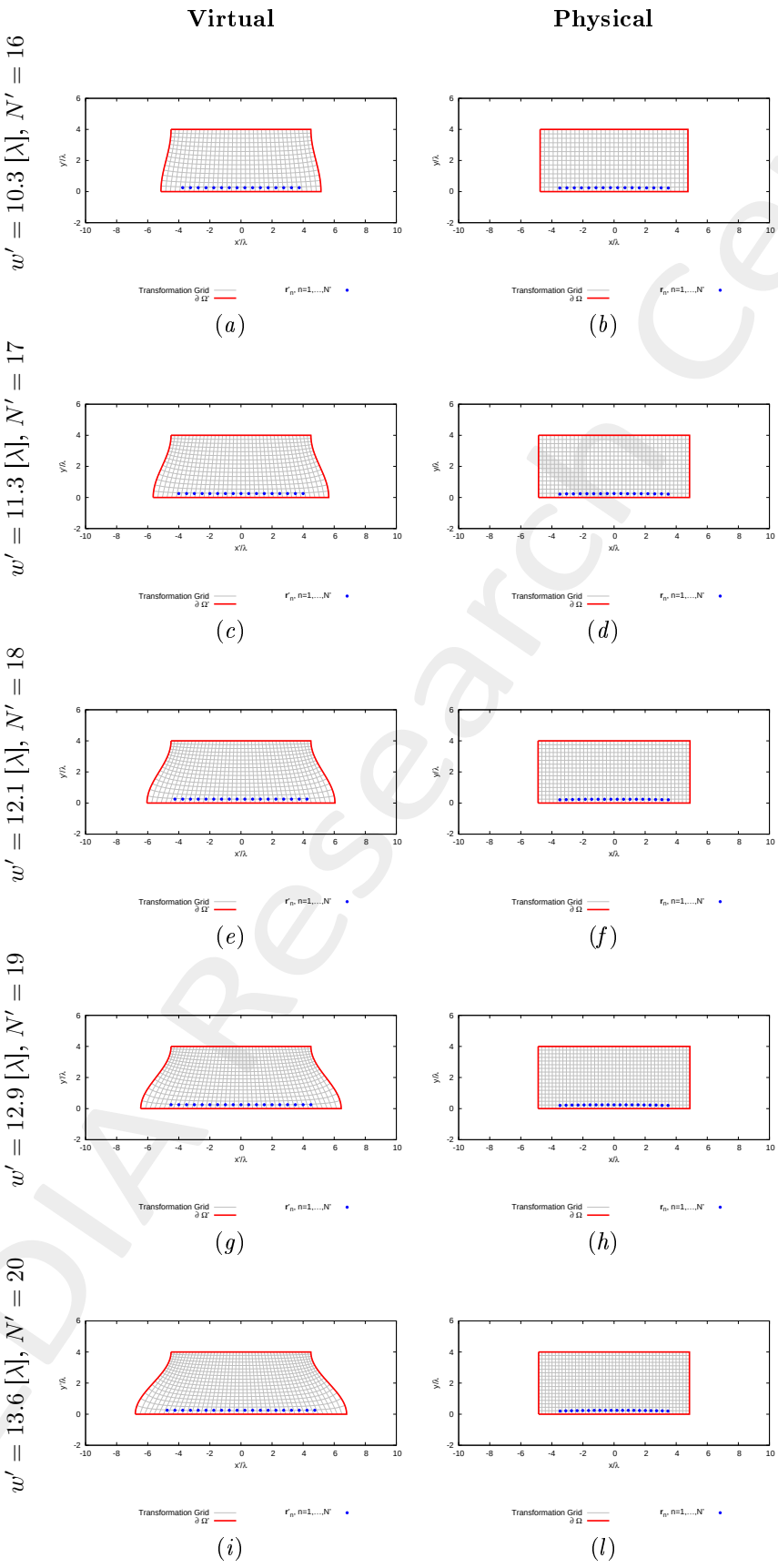

Figure 21: Transformation grids for different values of w'. Physical geometry has been shifted on y by $h/2 = 2.0$ $[\lambda]$.

Lens Permittivity - $w' = 10.3\ [\lambda]$

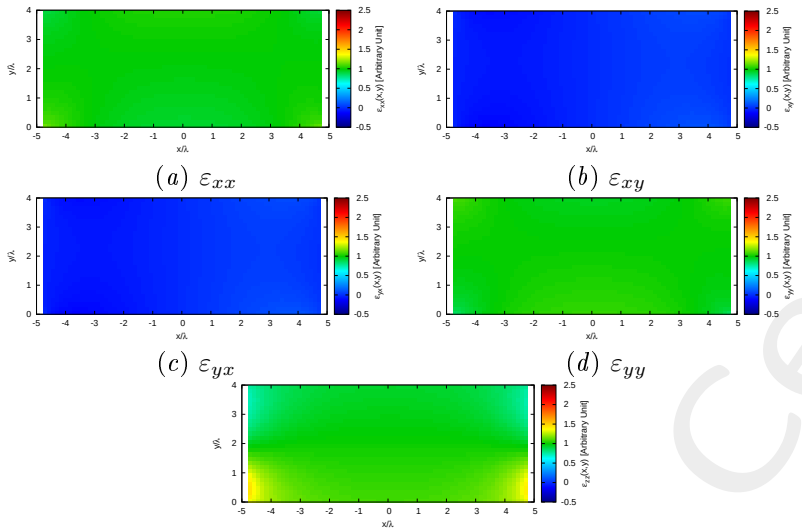

$(a)\ \varepsilon_{xx}$ $(b)\ \varepsilon_{xy}$ $(c)\ \varepsilon_{yx}$ $(d)\ \varepsilon_{yy}$ $(e)\ \varepsilon_{zz}$

Figure 22: Components of the relative permittivity tensor of the lens.

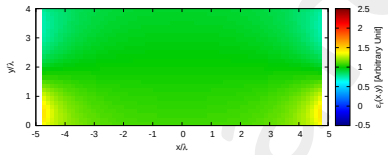

Figure 23: Isotropic approximate permittivity distribution of the lens.

Lens Permittivity - $w' = 11.3\ [\lambda]$

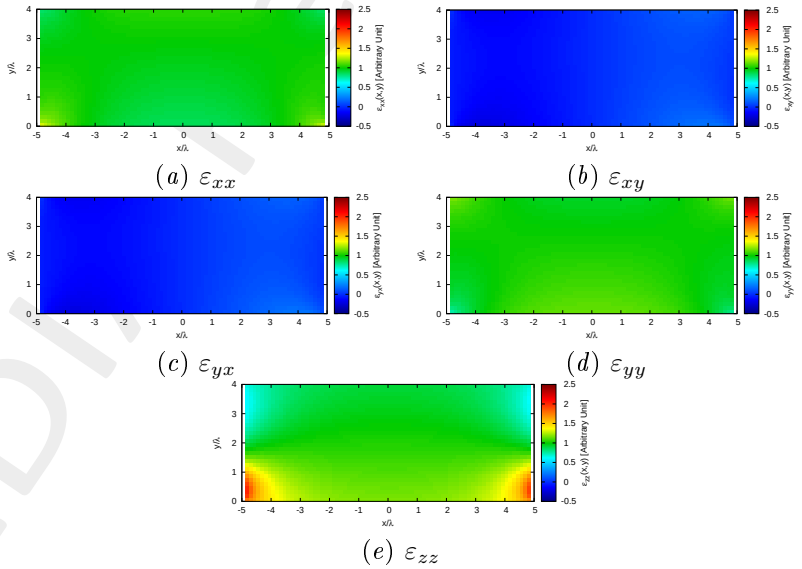

$(a)\ \varepsilon_{xx}$ $(b)\ \varepsilon_{xy}$ $(c)\ \varepsilon_{yx}$ $(d)\ \varepsilon_{yy}$ $(e)\ \varepsilon_{zz}$

Figure 24: Components of the relative permittivity tensor of the lens.

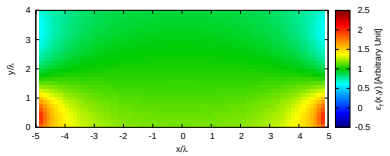

Figure 25: Isotropic approximate permittivity distribution of the lens.

Lens Permittivity - $w' = 12.1\ [\lambda]$

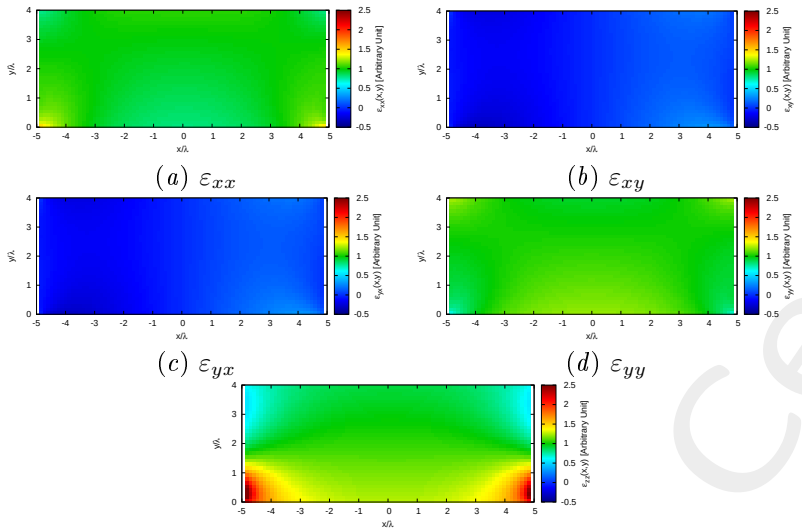

$(a)\ \varepsilon_{xx}$ $(b)\ \varepsilon_{xy}$ $(c)\ \varepsilon_{yx}$ $(d)\ \varepsilon_{yy}$ $(e)\ \varepsilon_{zz}$

Figure 26: Components of the relative permittivity tensor of the lens.

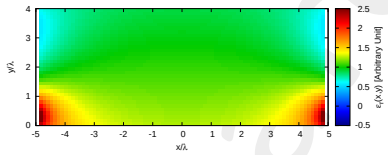

Figure 27: Isotropic approximate permittivity distribution of the lens.

Lens Permittivity - $w' = 12.9\ [\lambda]$

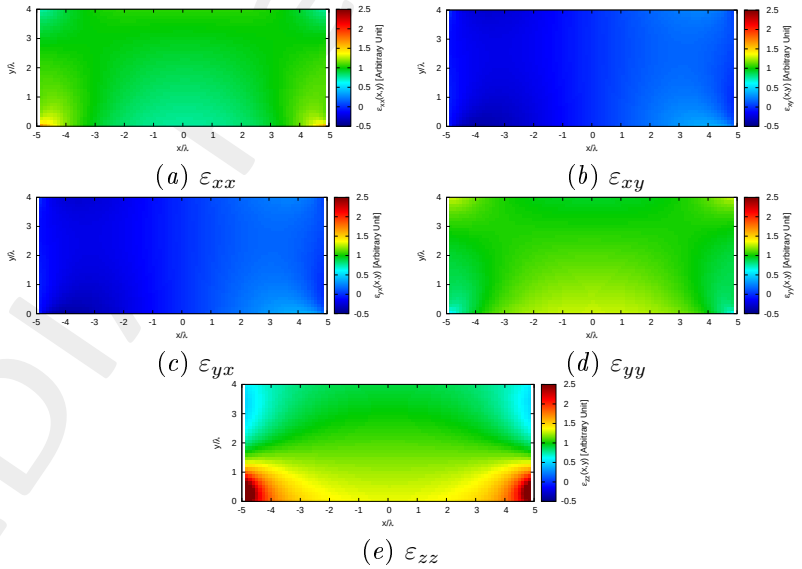

$(a)\ \varepsilon_{xx}$ $(b)\ \varepsilon_{xy}$ $(c)\ \varepsilon_{yx}$ $(d)\ \varepsilon_{yy}$ $(e)\ \varepsilon_{zz}$

Figure 28: Components of the relative permittivity tensor of the lens.

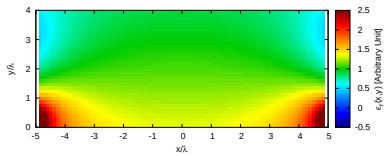

Figure 29: Isotropic approximate permittivity distribution of the lens.

Lens Permittivity - $w' = 13.6\ [\lambda]$

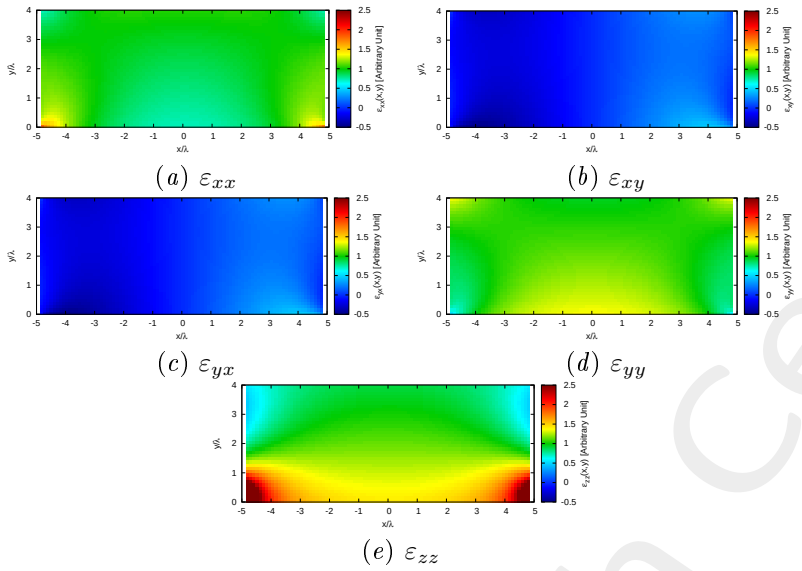

Figure 30: Components of the relative permittivity tensor of the lens.

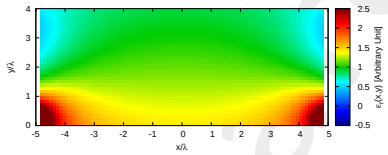

Figure 31: Isotropic approximate permittivity distribution of the lens.

Physical Lens Parameters

Parameter	$w' = 10.3\ [\lambda]$	$w' = 11.3\ [\lambda]$	$w' = 12.1\ [\lambda]$	$w' = 12.9\ [\lambda]$	$w' = 13.6\ [\lambda]$
Height, $h\ [\lambda]$	4.00	4.00	4.00	4.00	4.00
Width, $w\ [\lambda]$	9.51	9.72	9.78	9.76	9.71
Anisotropic Permittivity Range	$[-0.11, 1.46]$	$[-0.21, 2.03]$	$[-0.30, 2.67]$	$[-0.39, 3.51]$	$[-0.47, 4.43]$
Isotropic Permittivity Range	$[0.00, 1.44]$	$[0.00, 1.99]$	$[0.00, 2.59]$	$[0.00, 3.41]$	$[0.00, 4.35]$
Average Fractional Anisotropy, α_F	7.35×10^{-2}	1.28×10^{-1}	1.71×10^{-1}	2.12×10^{-1}	2.47×10^{-1}
Average Relative Anisotropy, α_R	6.06×10^{-2}	1.07×10^{-1}	1.46×10^{-1}	1.84×10^{-1}	2.19×10^{-1}

Table VIII: Transformation statistics. Note that we impose $h = h'$, while w is internally chosen by the QCTO software.

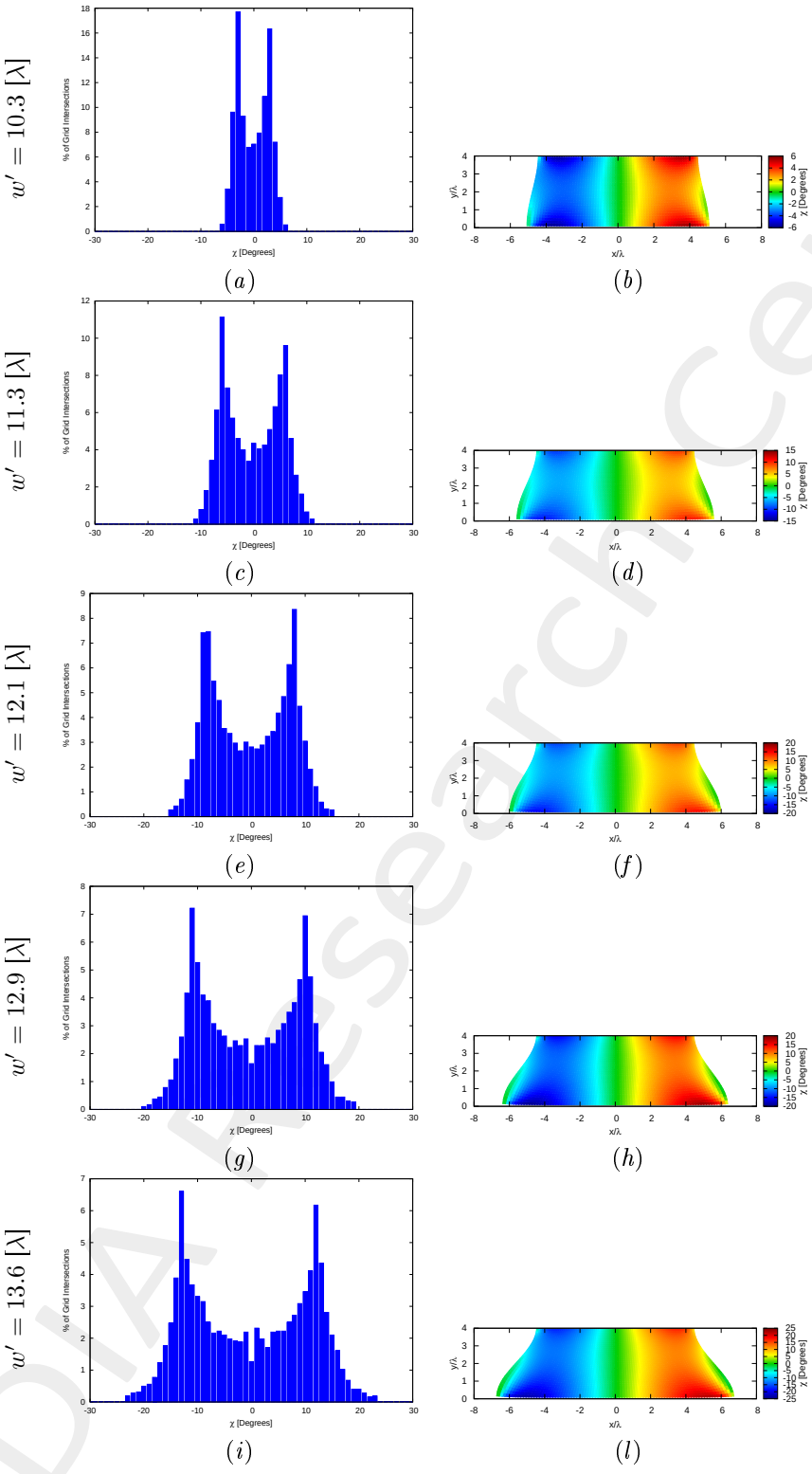

Figure 32: Orthogonality of the virtual grid for different values of w'.

2.2.2 Near-Field Distributions ($\phi_s = 90$ [deg], $f = 600$ [MHz])

Case $w' = 10.3$ [λ], $N' = 16$

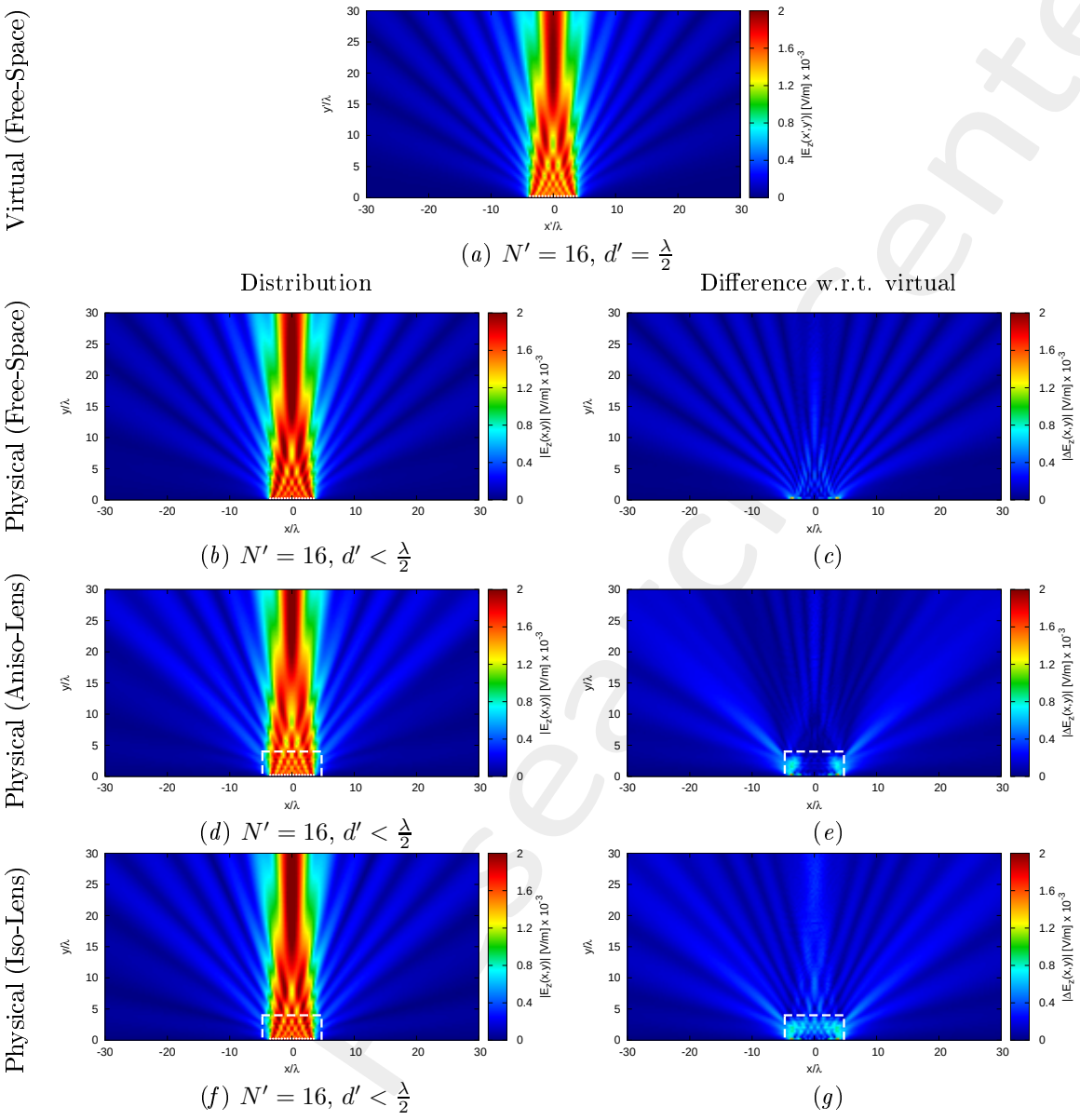

(a) $N' = 16$, $d' = \frac{\lambda}{2}$

(b) $N' = 16$, $d' < \frac{\lambda}{2}$ (c)

(d) $N' = 16$, $d' < \frac{\lambda}{2}$ (e)

(f) $N' = 16$, $d' < \frac{\lambda}{2}$ (g)

Figure 33: Electric field distributions.

Case $w' = 11.3$ **[**λ**],** $N' = 17$

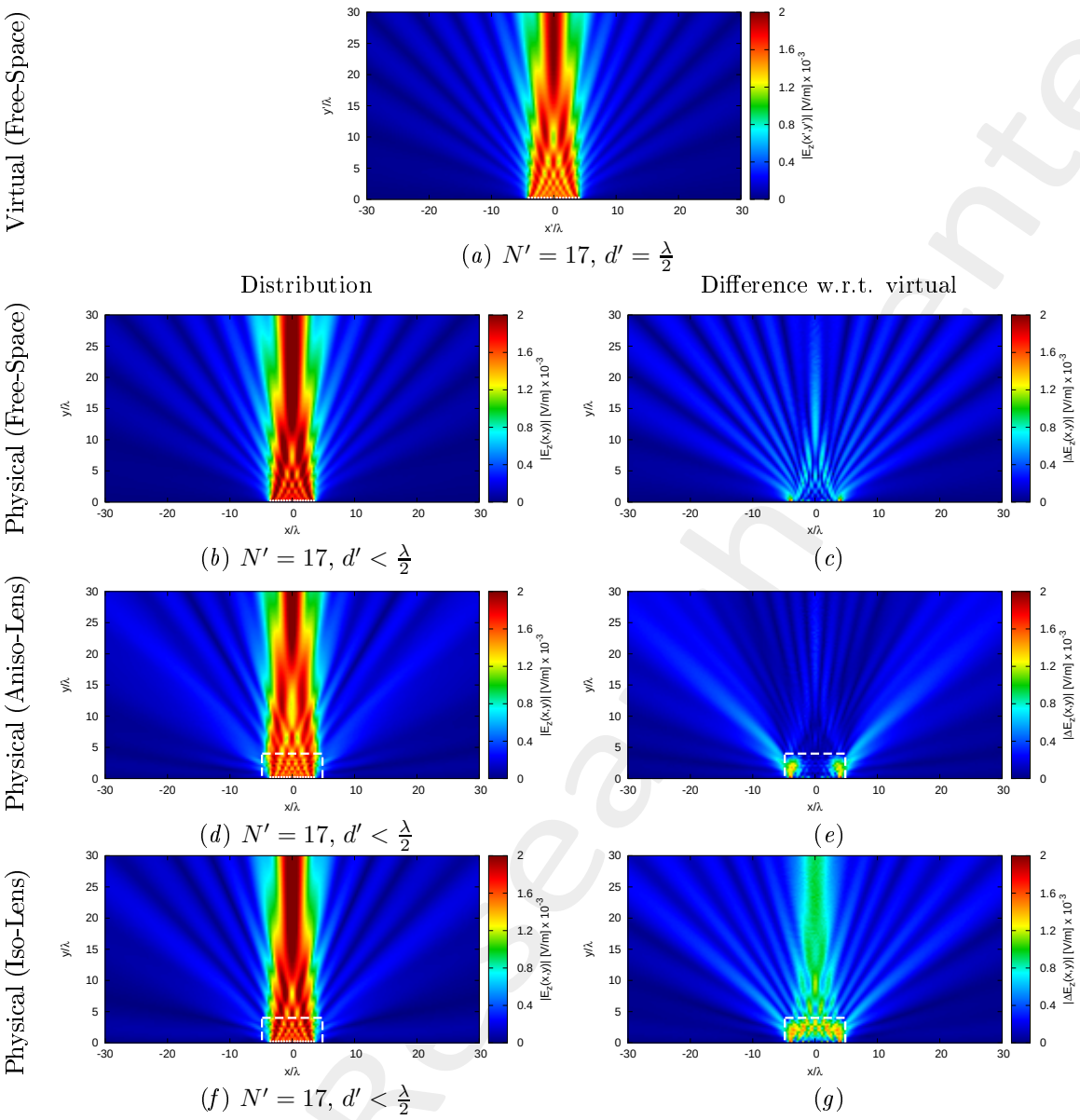

(a) $N' = 17$, $d' = \frac{\lambda}{2}$

(b) $N' = 17$, $d' < \frac{\lambda}{2}$ (c)

(d) $N' = 17$, $d' < \frac{\lambda}{2}$ (e)

(f) $N' = 17$, $d' < \frac{\lambda}{2}$ (g)

Figure 34: Electric field distributions.

Case $w' = 12.1$ **[**λ**],** $N' = 18$

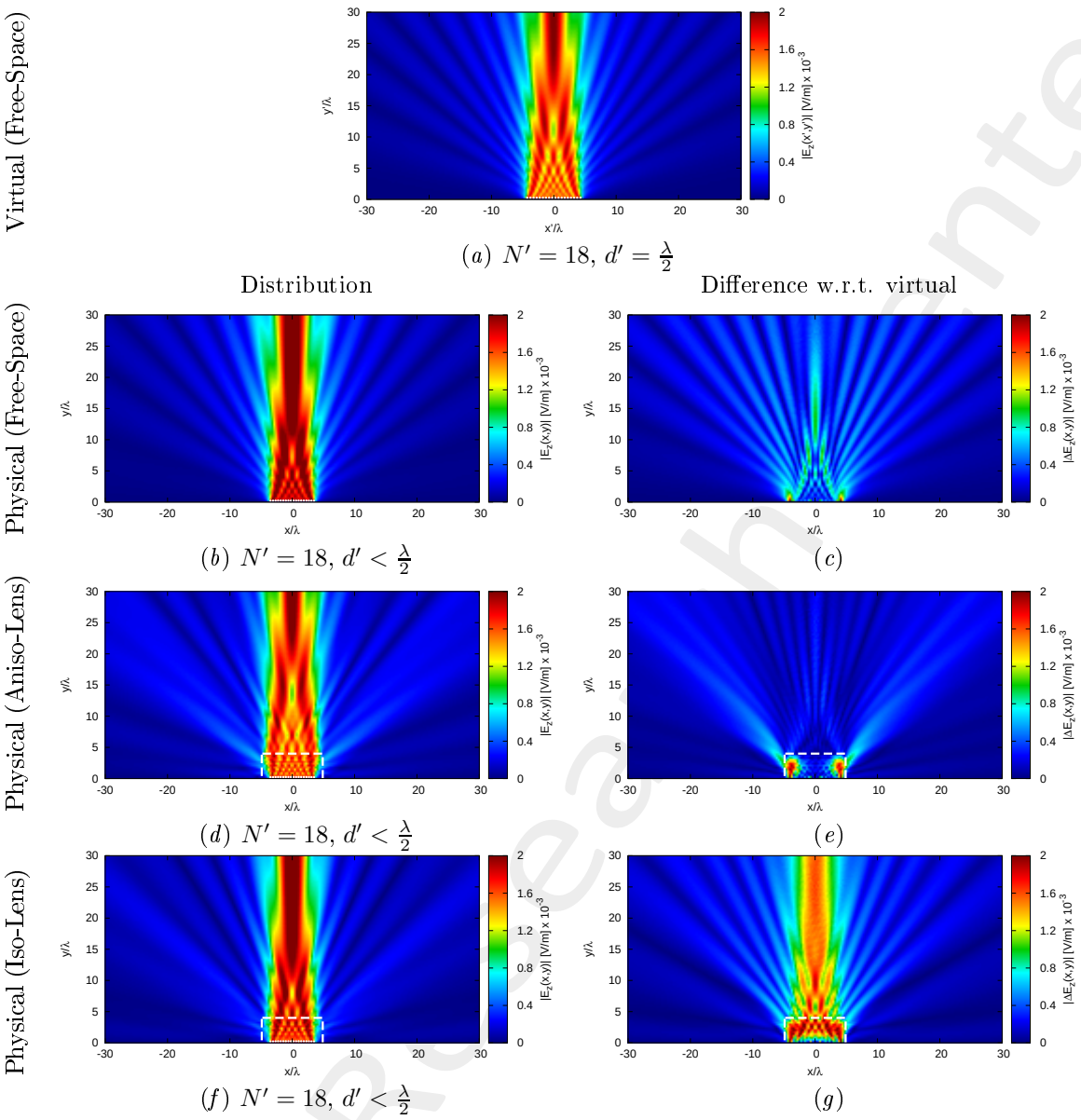

(a) $N' = 18$, $d' = \frac{\lambda}{2}$

(b) $N' = 18$, $d' < \frac{\lambda}{2}$ (c)

(d) $N' = 18$, $d' < \frac{\lambda}{2}$ (e)

(f) $N' = 18$, $d' < \frac{\lambda}{2}$ (g)

Figure 35: Electric field distributions.

Case $w' = 12.9$ **[**λ**],** $N' = 19$

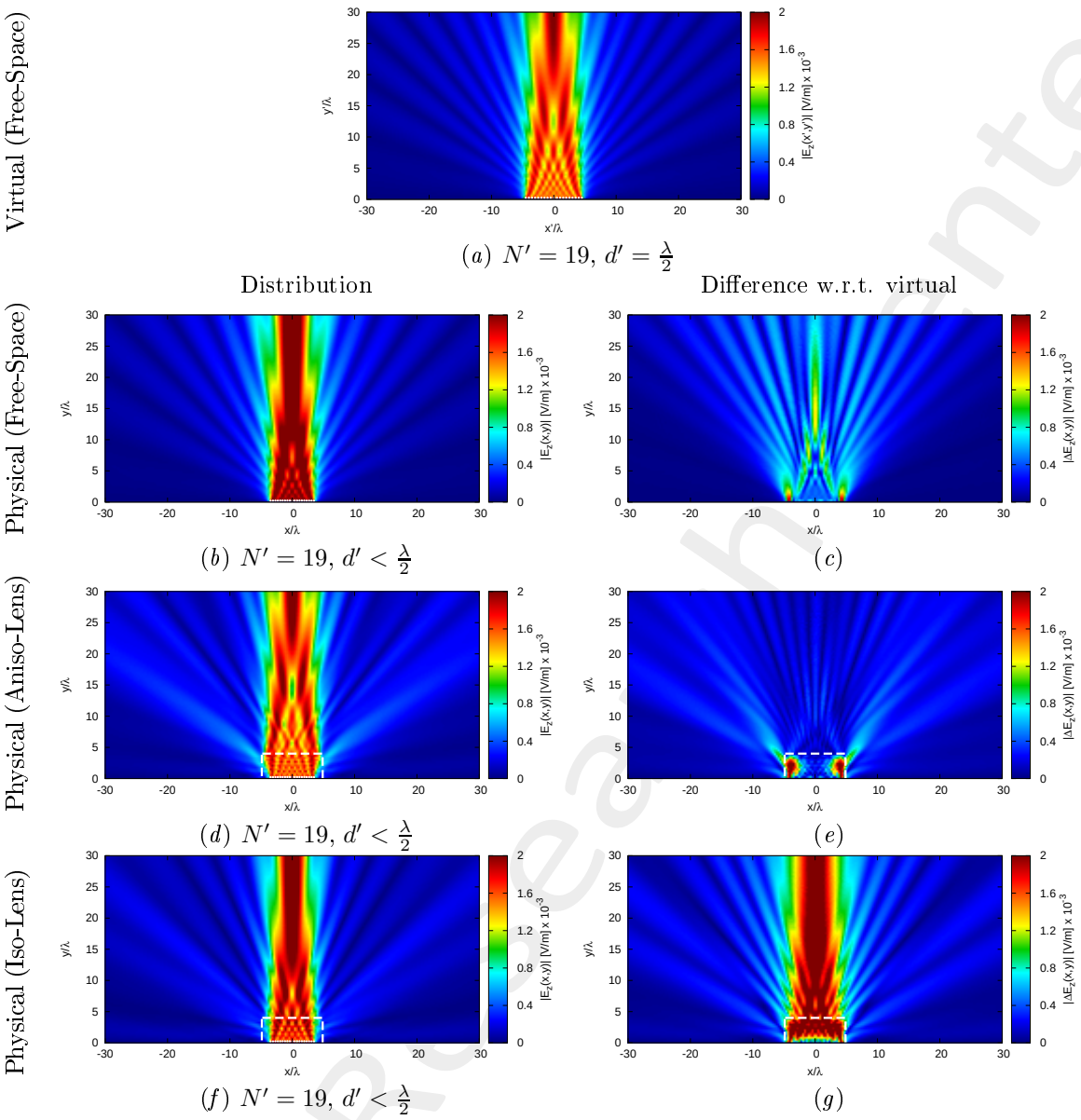

(a) $N' = 19$, $d' = \frac{\lambda}{2}$

(b) $N' = 19$, $d' < \frac{\lambda}{2}$ (c)

(d) $N' = 19$, $d' < \frac{\lambda}{2}$ (e)

(f) $N' = 19$, $d' < \frac{\lambda}{2}$ (g)

Figure 36: Electric field distributions.

Case $w' = 13.6$ **[**λ**],** $N' = 20$

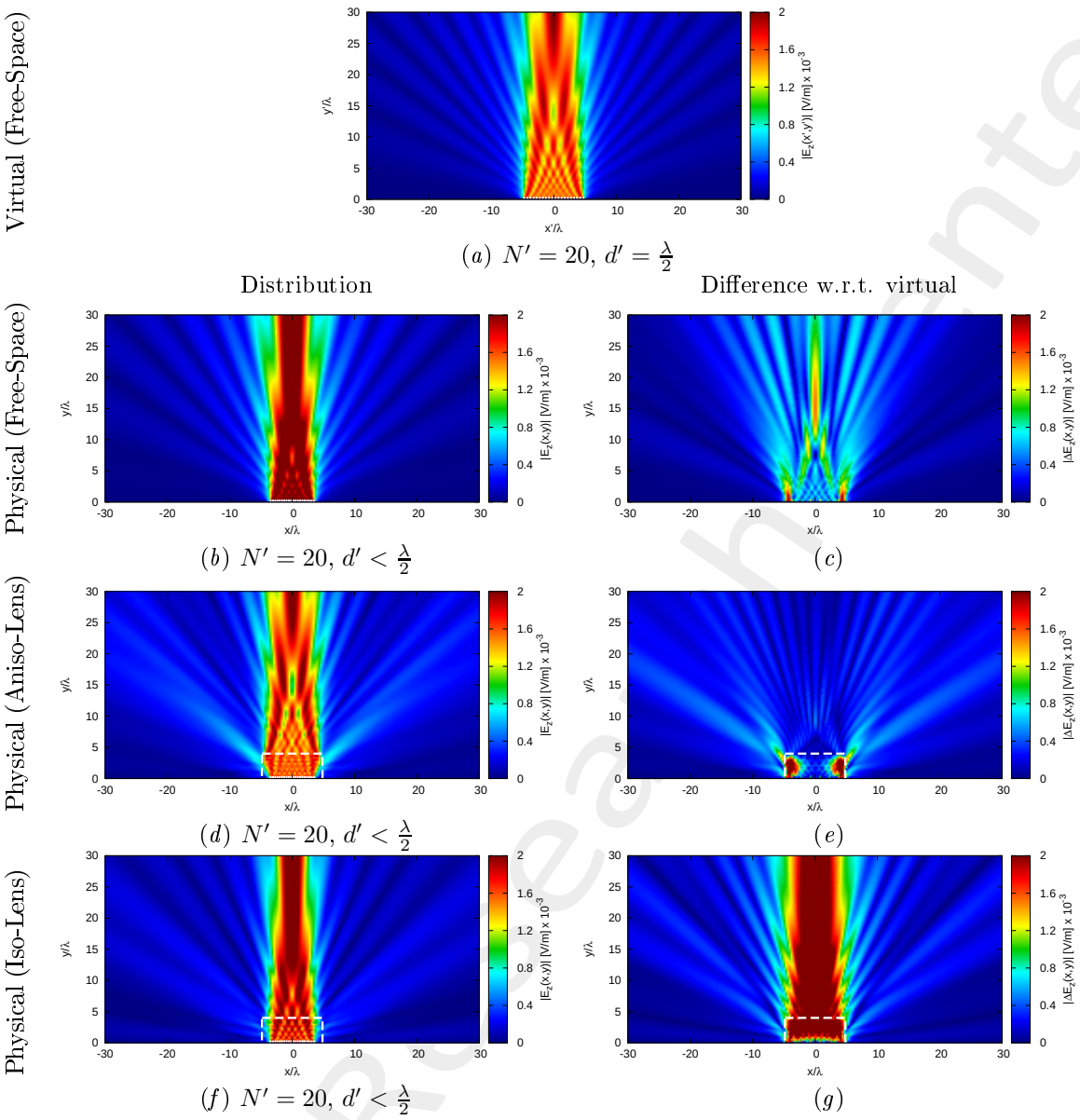

(a) $N' = 20$, $d' = \frac{\lambda}{2}$

(b) $N' = 20$, $d' < \frac{\lambda}{2}$ (c)

(d) $N' = 20$, $d' < \frac{\lambda}{2}$ (e)

(f) $N' = 20$, $d' < \frac{\lambda}{2}$ (g)

Figure 37: Electric field distributions.

2.2.3 Far-Field Patterns ($\phi_s = 90$ [deg], $f = 600$ [MHz])

Anisotropic Lens

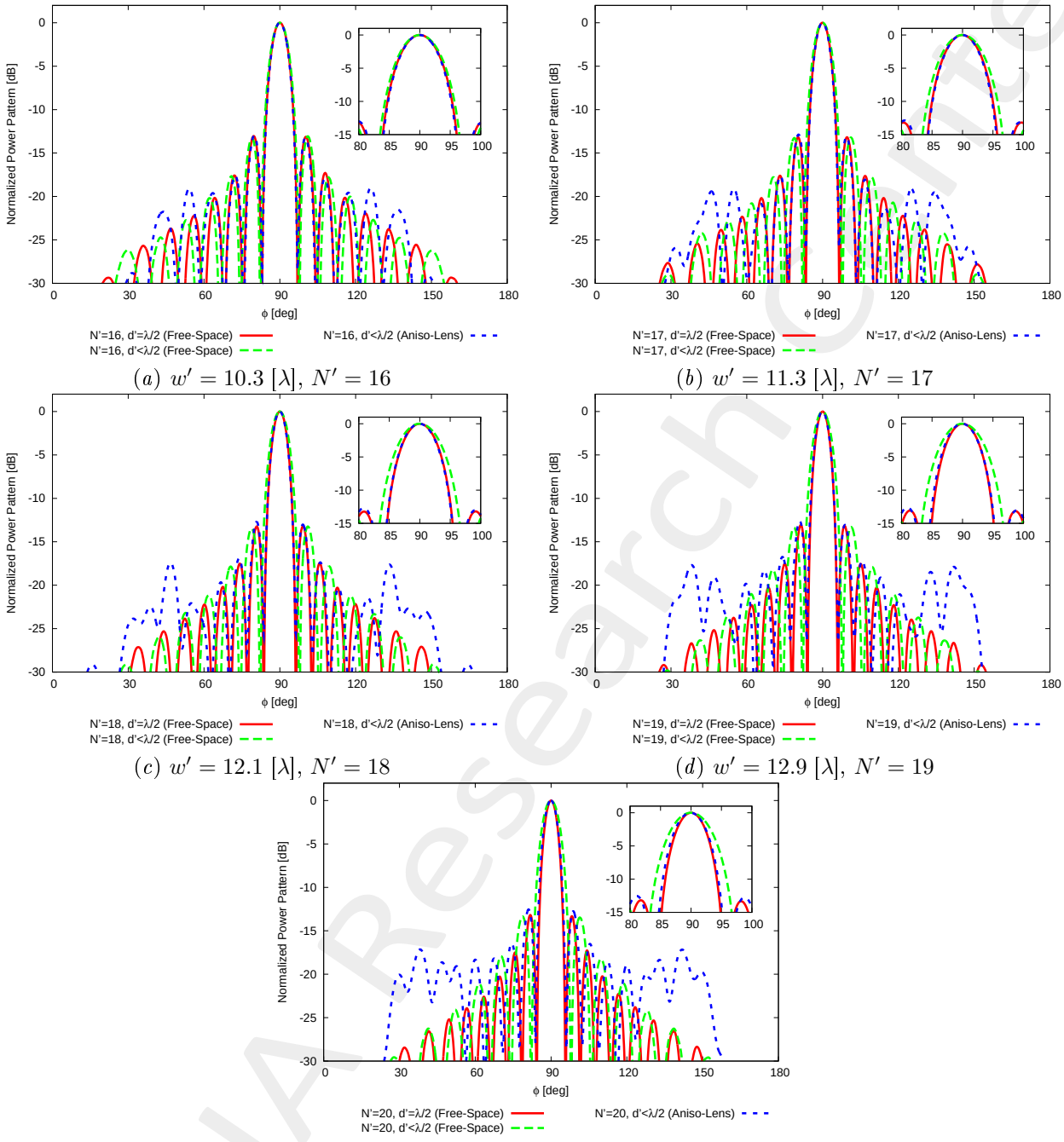

(a) $w' = 10.3$ $[\lambda]$, $N' = 16$

(b) $w' = 11.3$ $[\lambda]$, $N' = 17$

(c) $w' = 12.1$ $[\lambda]$, $N' = 18$

(d) $w' = 12.9$ $[\lambda]$, $N' = 19$

(e) $w' = 13.6$ $[\lambda]$, $N' = 20$

Figure 38: Far field pattern comparison for different values of w'.

Isotropic Lens

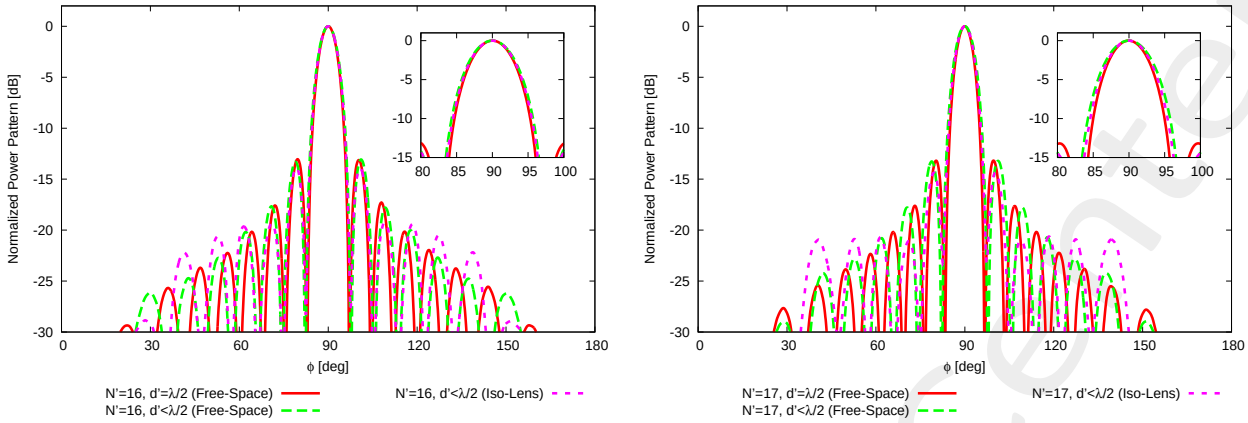

(a) $w' = 10.3$ $[\lambda]$, $N' = 16$

(b) $w' = 11.3$ $[\lambda]$, $N' = 17$

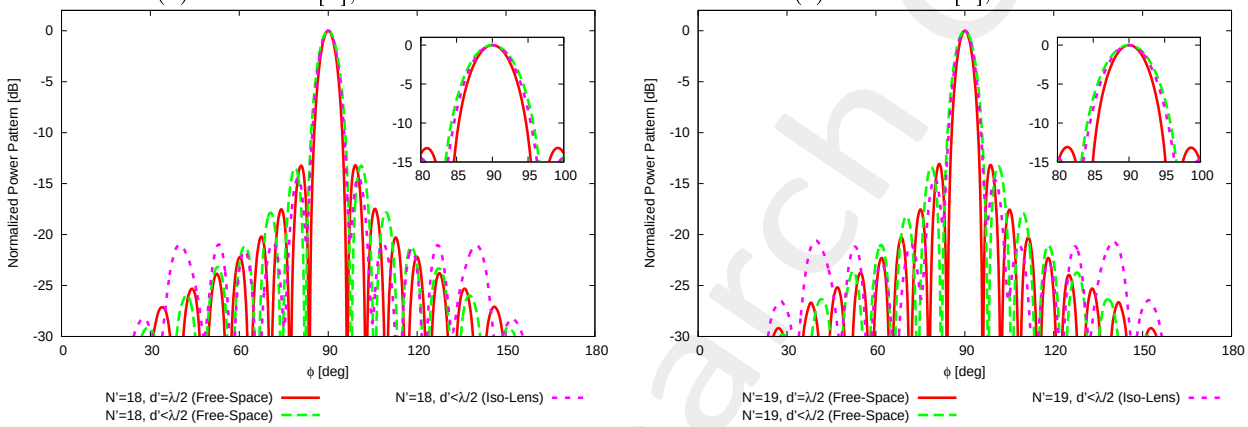

(c) $w' = 12.1$ $[\lambda]$, $N' = 18$

(d) $w' = 12.9$ $[\lambda]$, $N' = 19$

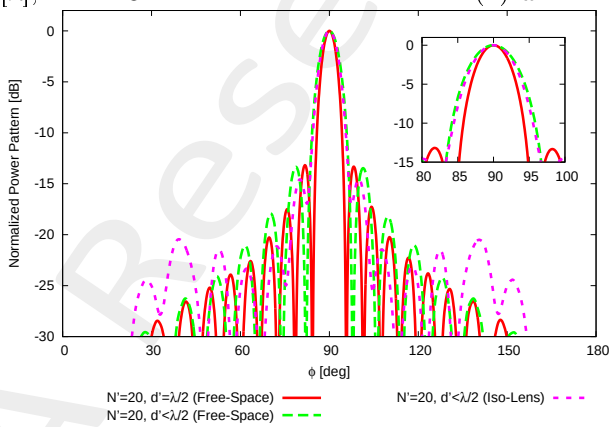

(e) $w' = 13.6$ $[\lambda]$, $N' = 20$

Figure 39: Far field pattern comparison for different values of w'.

2.2.4 Summary ($\phi_s = 90$ [deg], $f = 600$ [MHz])

$w' = 10.3$ [λ]				
	Virtual Array	**Physical Array**		
Environment	Free-Space	Free-Space	Aniso-Lens	Iso-Lens
Number of elements	16	16		
Spacing [λ]	0.5	< 0.5		
Aperture [λ]	7.5	6.98		
$D_{\max}$ [dB]	13.97	13.70	13.98	13.83
SLL [dB]	13.11	13.07	13.00	13.88
$FNBW$ [deg]	14.32	15.40	14.05	15.04
3dB Beamwidth [deg]	6.36	6.81	6.2	6.57
Matching Error, ξ (w.r.t. virtual, outside lens)	-	3.59×10^{-1}	4.36×10^{-1}	5.36×10^{-1}

$w' = 11.3$ [λ]				
	Virtual Array	**Physical Array**		
Environment	Free-Space	Free-Space	Aniso-Lens	Iso-Lens
Number of elements	17	17		
Spacing [λ]	0.5	< 0.5		
Aperture [λ]	8.0	6.97		
$D_{\max}$ [dB]	14.25	13.67	14.19	13.96
SLL [dB]	13.16	13.21	12.88	14.33
$FNBW$ [deg]	13.60	15.58	13.24	14.86
3dB Beamwidth [deg]	5.97	6.89	5.82	6.39
Matching Error, ξ (w.r.t. virtual, outside lens)	-	6.05×10^{-1}	5.57×10^{-1}	8.19×10^{-1}

$w' = 12.1$ [λ]				
	Virtual Array	**Physical Array**		
Environment	Free-Space	Free-Space	Aniso-Lens	Iso-Lens
Number of elements	18	18		
Spacing [λ]	0.5	< 0.5		
Aperture [λ]	8.5	6.98		
$D_{\max}$ [dB]	14.50	13.70	14.27	13.99
SLL [dB]	13.14	13.24	12.69	14.37
$FNBW$ [deg]	12.79	15.58	12.70	14.68
3dB Beamwidth [deg]	5.64	6.86	5.62	6.32
Matching Error, ξ (w.r.t. virtual, outside lens)	-	6.94×10^{-1}	5.49×10^{-1}	1.03

$w' = 12.9$ [λ]				
	Virtual Array	**Physical Array**		
Environment	Free-Space	Free-Space	Aniso-Lens	Iso-Lens
Number of elements	19	19		
Spacing [λ]	0.5	< 0.5		
Aperture [λ]	9.0	6.95		
$D_{\max}$ [dB]	14.73	13.65	14.24	13.93
SLL [dB]	13.06	13.30	12.61	14.49
$FNBW$ [deg]	12.07	15.76	12.43	14.86
3dB Beamwidth [deg]	5.35	6.96	5.49	6.38
Matching Error, ξ (w.r.t. virtual, outside lens)	-	6.90×10^{-1}	6.33×10^{-1}	1.31

$w' = 13.6$ [λ]				
	Virtual Array	**Physical Array**		
Environment	Free-Space	Free-Space	Aniso-Lens	Iso-Lens
Number of elements	20	20		
Spacing [λ]	0.5	< 0.5		
Aperture [λ]	9.5	6.94		
$D_{\max}$ [dB]	14.96	13.63	14.15	13.87
SLL [dB]	13.18	13.35	12.54	14.54
$FNBW$ [deg]	11.44	15.85	12.25	15.04
3dB Beamwidth [deg]	5.06	7.00	5.45	6.43
Matching Error, ξ (w.r.t. virtual, outside lens)	-	7.26×10^{-1}	7.03×10^{-1}	1.48

Table IX: Summary for step 2.

2.3 Source Inversion (SI)

Parameters

- Before SI
  - Number of elements: $N' = \{16; 17; 18; 19; 20\}$, $d' < \lambda/2$;
- After SI
  - Number of elements after SI: $N = 15$, $d = \frac{\lambda}{2}$;
  - Aperture: $L = 7.0$;
- Radius of the observation domain: $r_{SI} = 50.0$ [λ];
- Number of field sampling points: $n_{SI} = 1000$.

2.3.1 Results of the SI ($\phi_s = 90$ [deg], $f = 600$ [MHz])

Synthesized Excitations

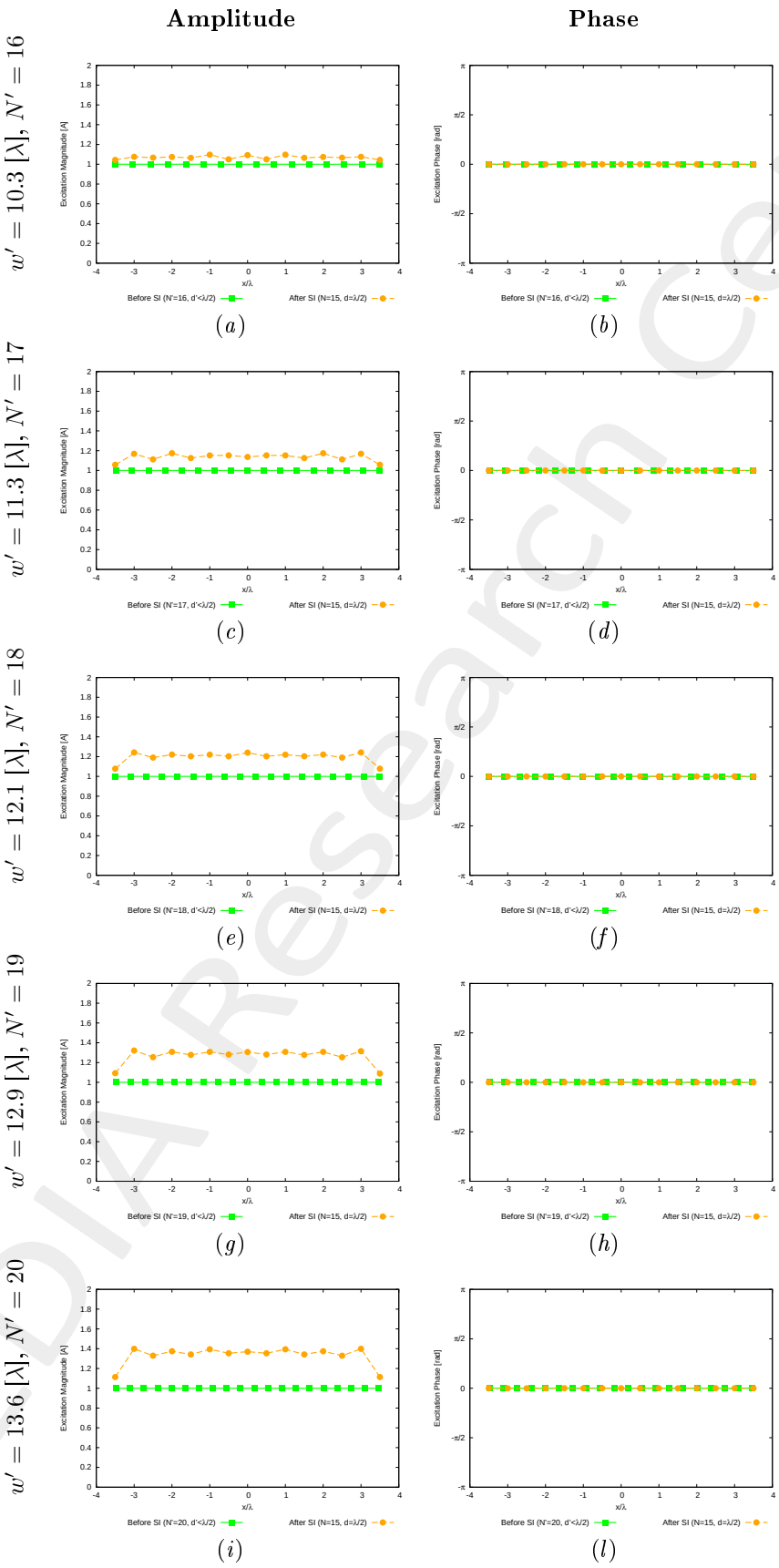

Figure 40: $\phi_s = 90$ [deg], $f = 600$ [MHz] - Synthesized excitations through SI.

Check SI: Free-Space Patterns

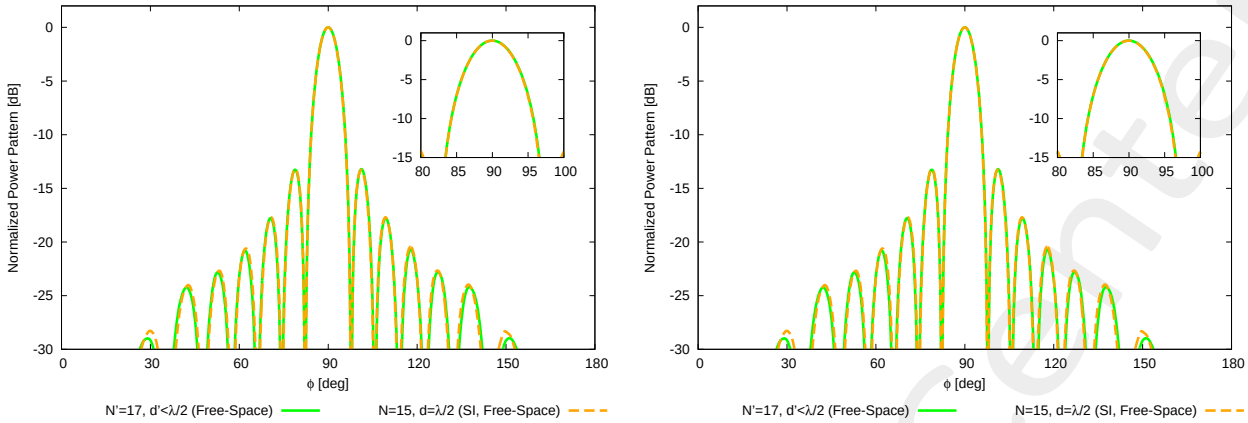

(a) $w' = 10.3$ [λ], $N' = 16$ (b) $w' = 11.3$ [λ], $N' = 17$

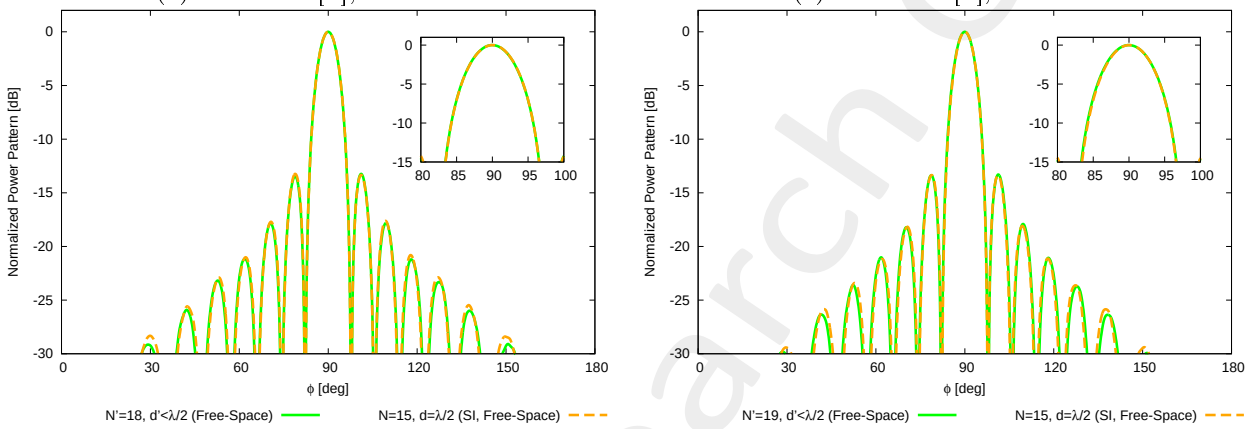

(c) $w' = 12.1$ [λ], $N' = 18$ (d) $w' = 12.9$ [λ], $N' = 19$

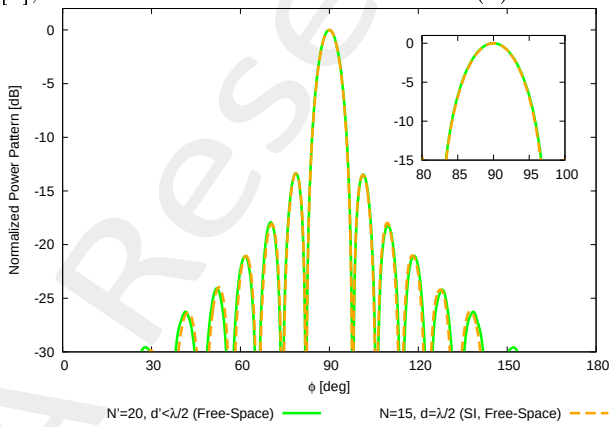

(e) $w' = 13.6$ [λ], $N' = 20$

Figure 41: $\phi_s = 90$ [deg], $f = 600$ [MHz] - Free-space far field pattern comparison for different values of w'.

2.3.2 Near-Field Distribution ($\phi_s = 90$ [deg], $f = 600$ [MHz])

Case $w' = 10.3$ [λ], $N' = 16$

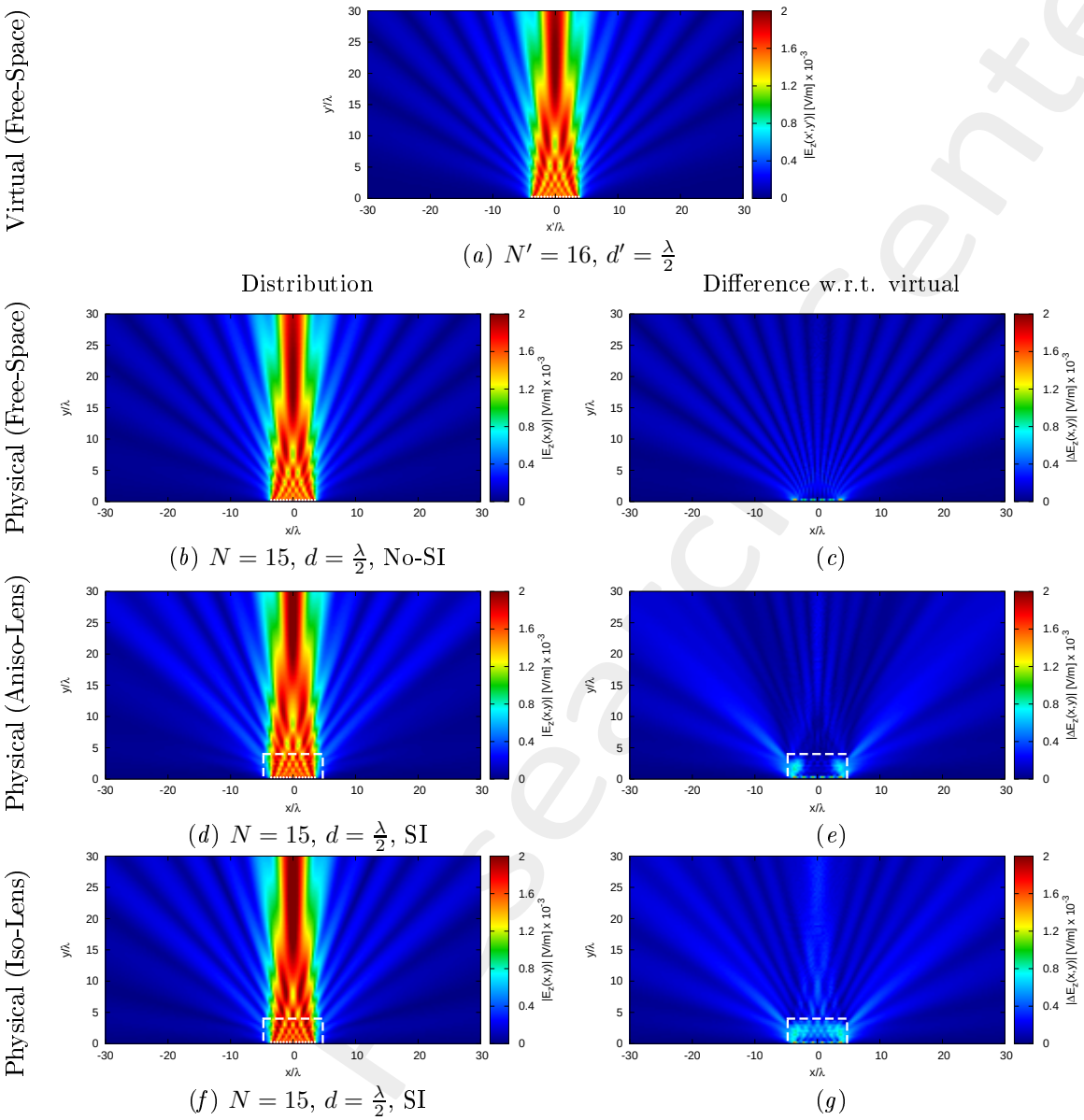

(a) $N' = 16$, $d' = \frac{\lambda}{2}$

(b) $N = 15$, $d = \frac{\lambda}{2}$, No-SI (c)

(d) $N = 15$, $d = \frac{\lambda}{2}$, SI (e)

(f) $N = 15$, $d = \frac{\lambda}{2}$, SI (g)

Figure 42: $\phi_s = 90$ [deg], $f = 600$ [MHz] - Electric field distributions.

Case $w' = 11.3$ **[**λ**],** $N' = 17$

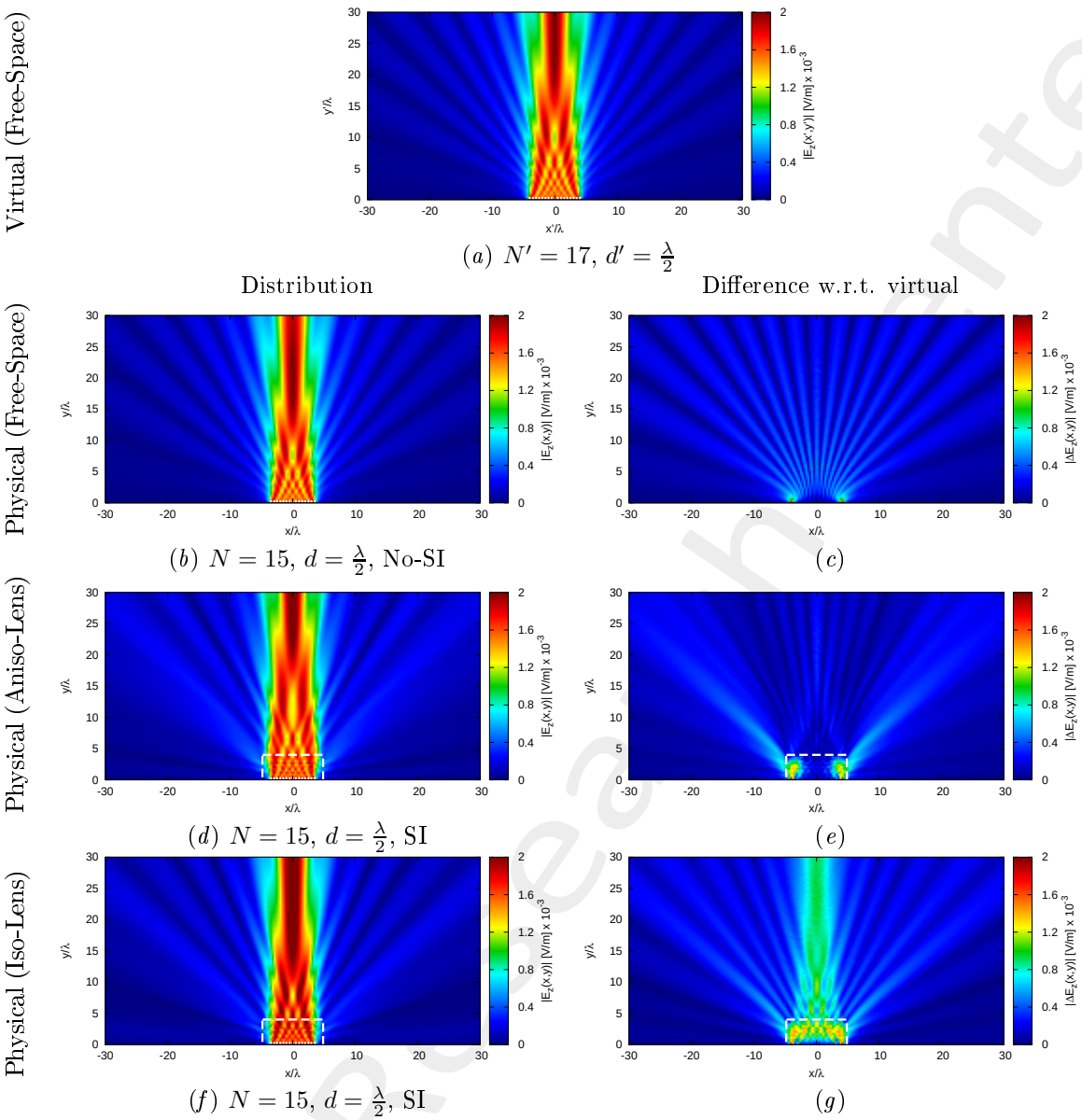

(a) $N' = 17$, $d' = \frac{\lambda}{2}$

(b) $N = 15$, $d = \frac{\lambda}{2}$, No-SI (c)

(d) $N = 15$, $d = \frac{\lambda}{2}$, SI (e)

(f) $N = 15$, $d = \frac{\lambda}{2}$, SI (g)

Figure 43: $\phi_s = 90$ [deg], $f = 600$ [MHz] - Electric field distributions.

Case $w' = 12.1$ **[**λ**],** $N' = 18$

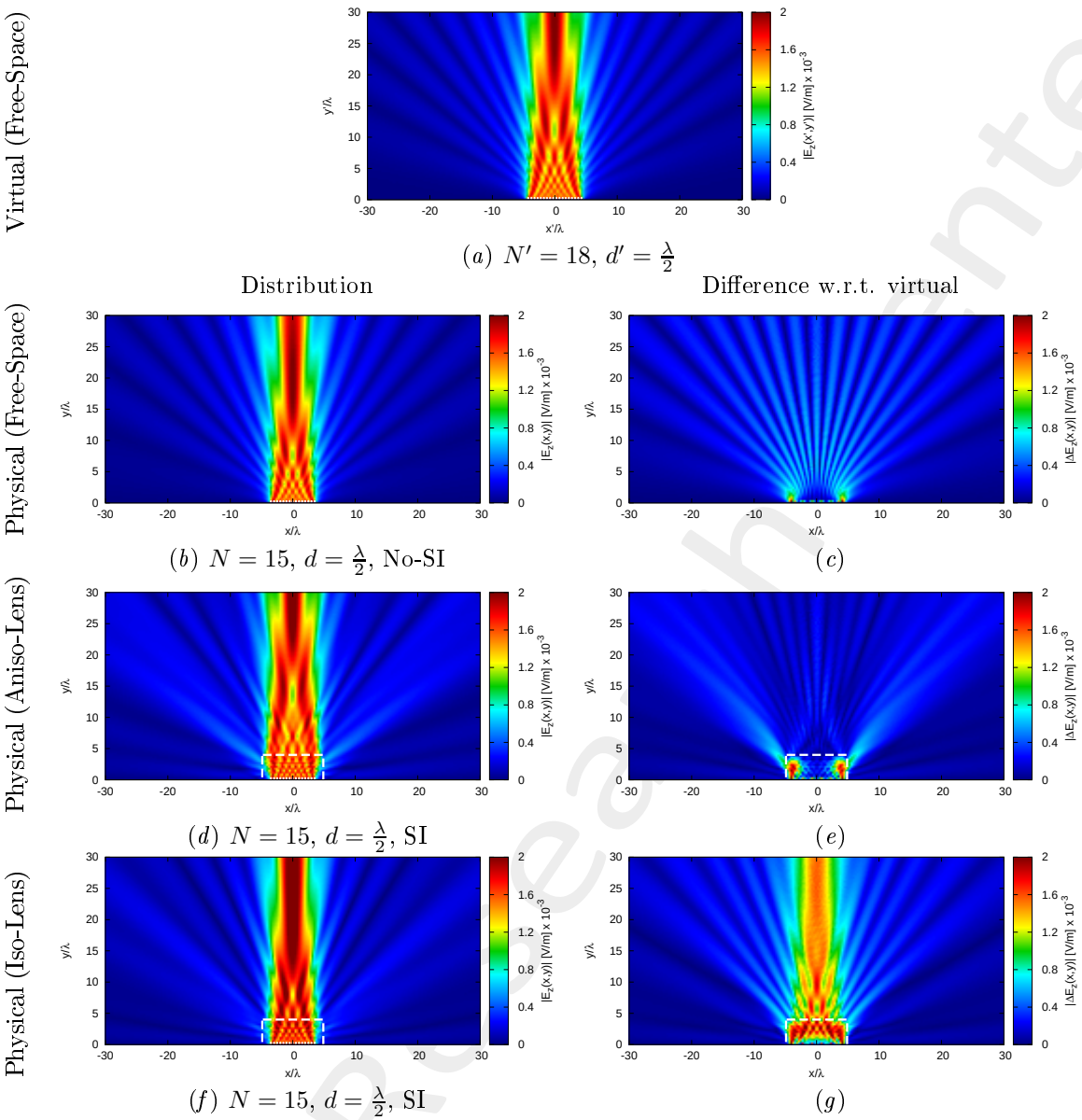

(a) $N' = 18$, $d' = \frac{\lambda}{2}$

(b) $N = 15$, $d = \frac{\lambda}{2}$, No-SI (c)

(d) $N = 15$, $d = \frac{\lambda}{2}$, SI (e)

(f) $N = 15$, $d = \frac{\lambda}{2}$, SI (g)

Figure 44: $\phi_s = 90$ [deg], $f = 600$ [MHz] - Electric field distributions.

Case $w' = 12.9$ **[**λ**],** $N' = 19$

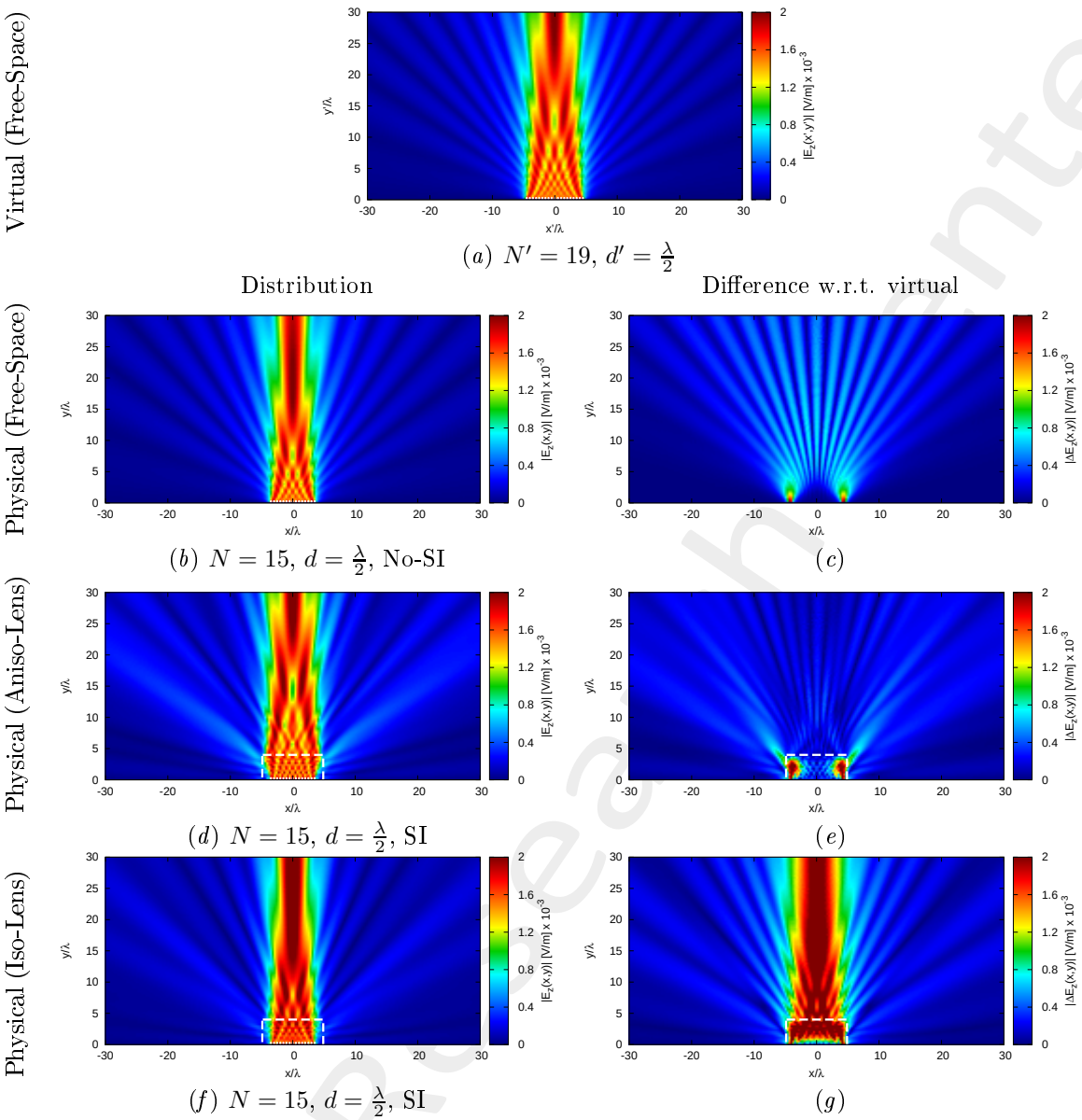

(a) $N' = 19$, $d' = \frac{\lambda}{2}$

(b) $N = 15$, $d = \frac{\lambda}{2}$, No-SI (c)

(d) $N = 15$, $d = \frac{\lambda}{2}$, SI (e)

(f) $N = 15$, $d = \frac{\lambda}{2}$, SI (g)

Figure 45: $\phi_s = 90$ [deg], $f = 600$ [MHz] - Electric field distributions.

Case $w' = 13.6$ **[**λ**],** $N' = 20$

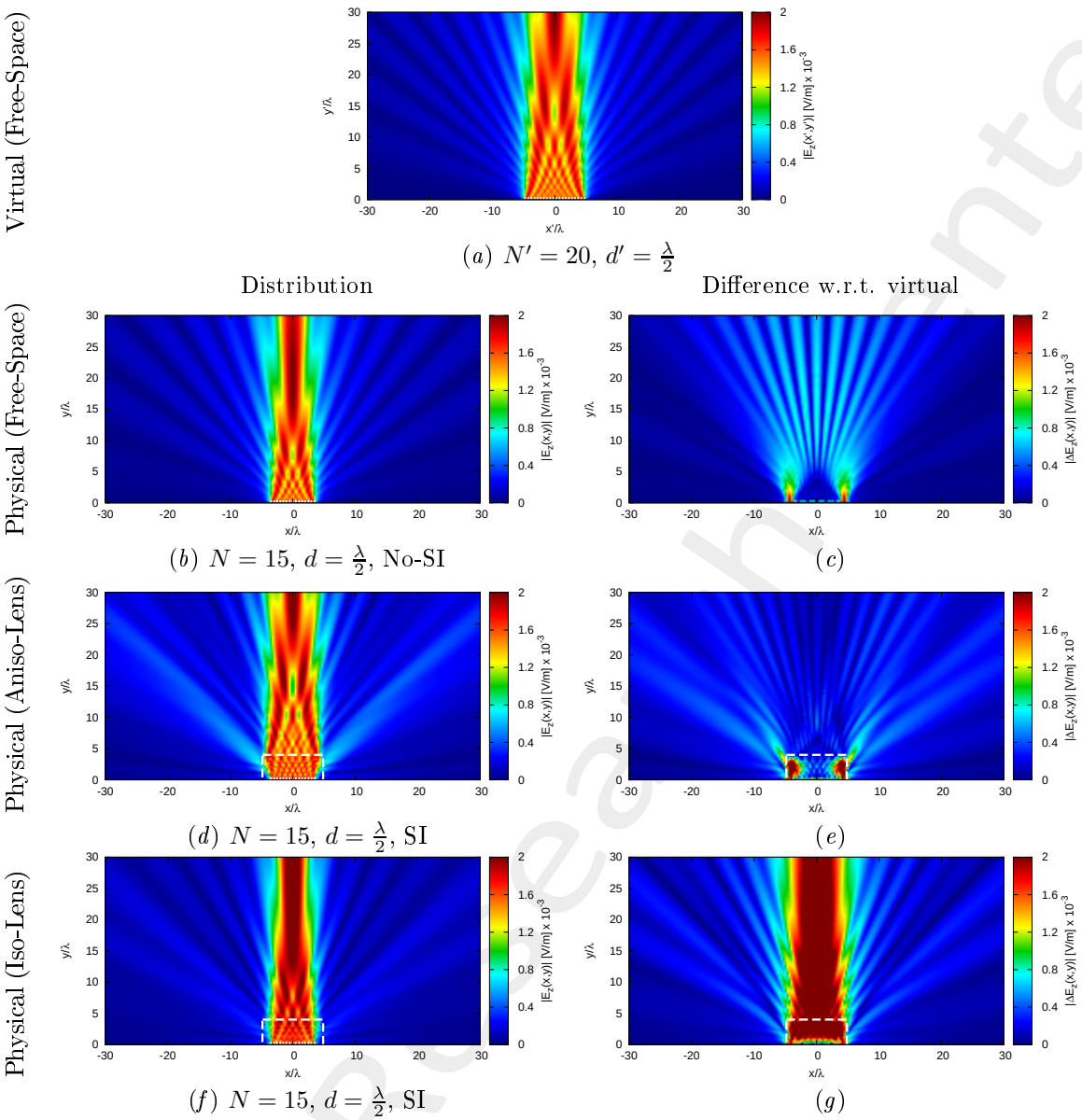

(a) $N' = 20$, $d' = \frac{\lambda}{2}$

(b) $N = 15$, $d = \frac{\lambda}{2}$, No-SI (c)

(d) $N = 15$, $d = \frac{\lambda}{2}$, SI (e)

(f) $N = 15$, $d = \frac{\lambda}{2}$, SI (g)

Figure 46: $\phi_s = 90$ [deg], $f = 600$ [MHz] - Electric field distributions.

2.3.3 Far-Field Patterns ($\phi_s = 90$ [deg], $f = 600$ [MHz])

Anisotropic Lens

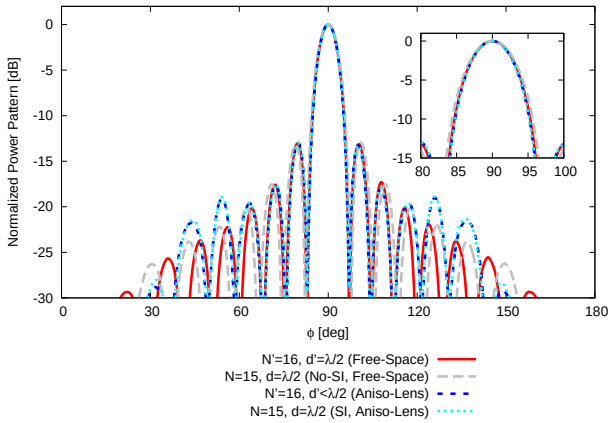

(a) $w' = 10.3$ [λ], $N' = 16$

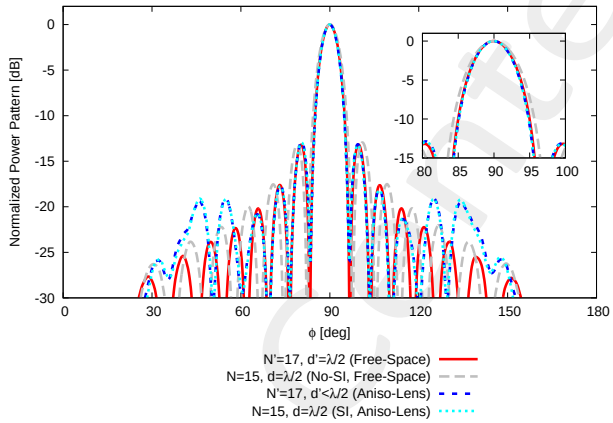

(b) $w' = 11.3$ [λ], $N' = 17$

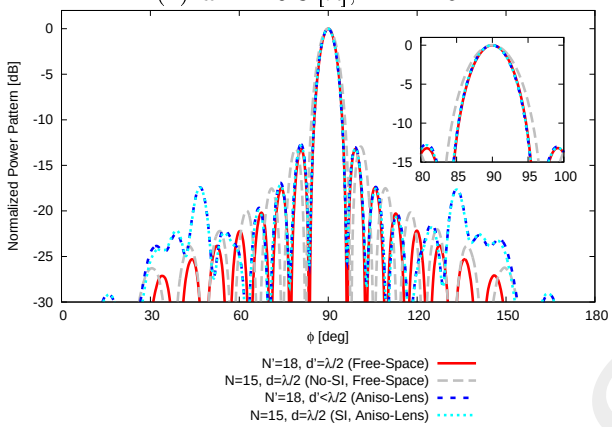

(c) $w' = 12.1$ [λ], $N' = 18$

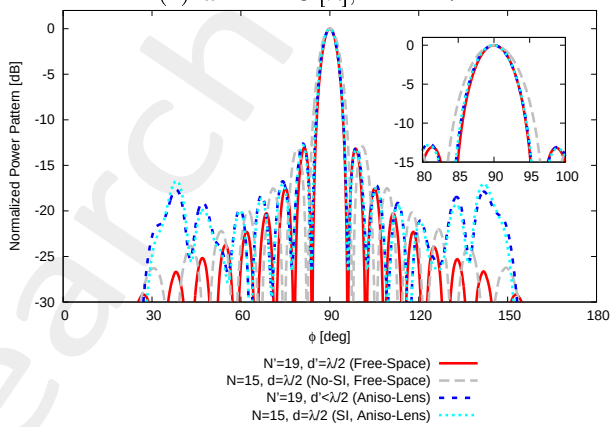

(d) $w' = 12.9$ [λ], $N' = 19$

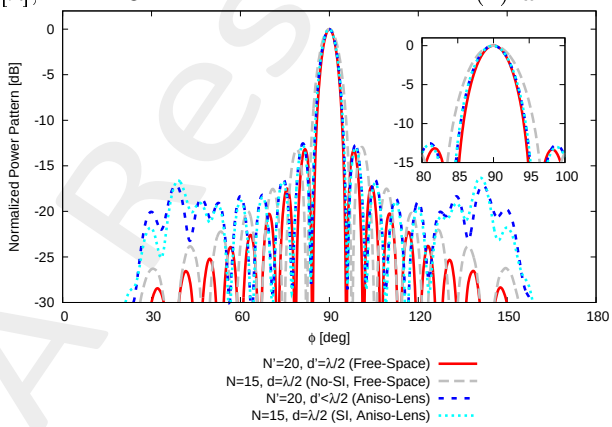

(e) $w' = 13.6$ [λ], $N' = 20$

Figure 47: $\phi_s = 90$ [deg], $f = 600$ [MHz] - Far field pattern comparison for different values of w'.

Isotropic Lens

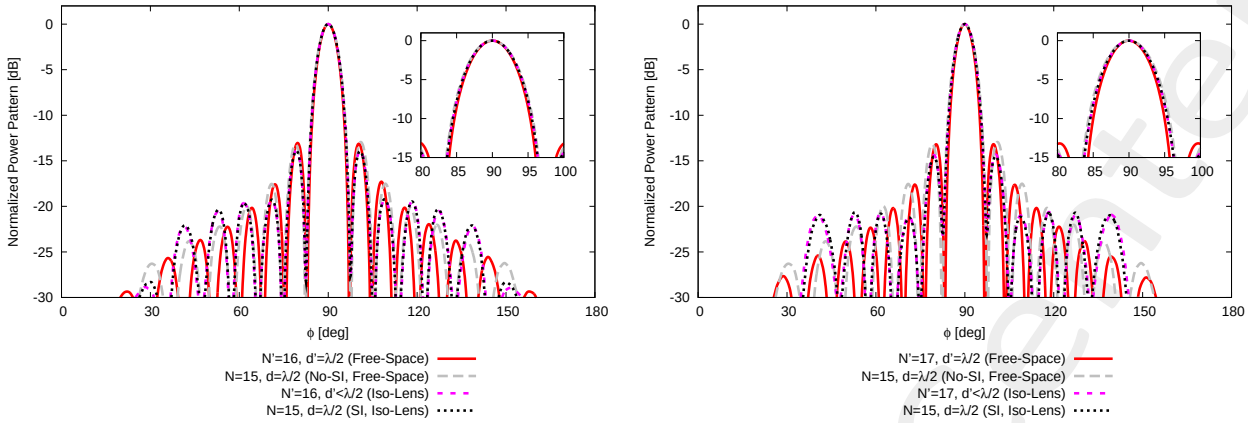

(a) $w' = 10.3$ $[\lambda]$, $N' = 16$

(b) $w' = 11.3$ $[\lambda]$, $N' = 17$

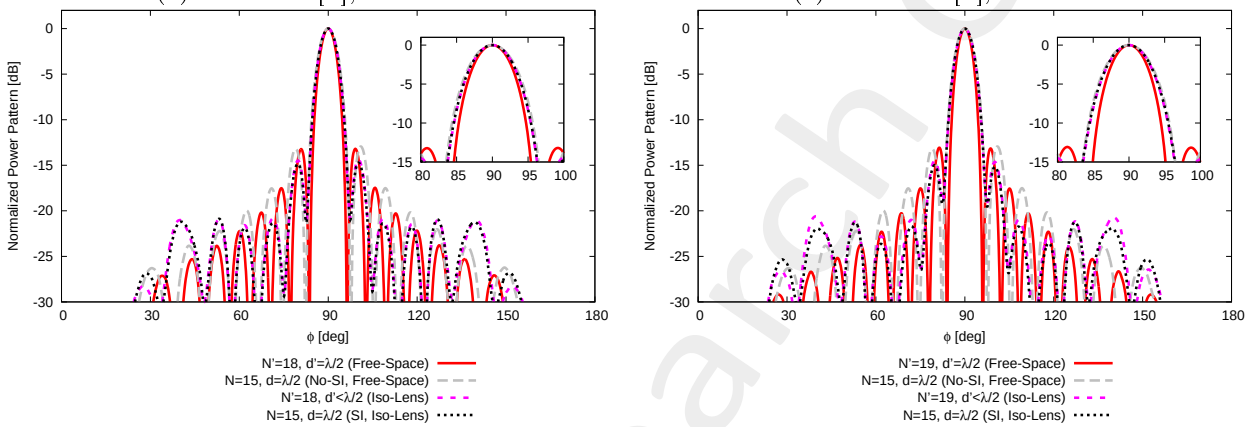

(c) $w' = 12.1$ $[\lambda]$, $N' = 18$

(d) $w' = 12.9$ $[\lambda]$, $N' = 19$

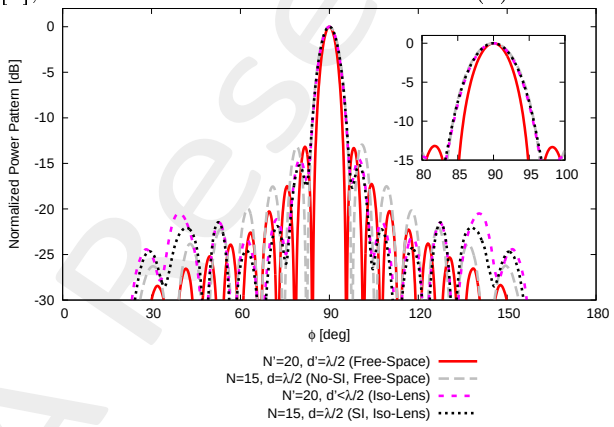

(e) $w' = 13.6$ $[\lambda]$, $N' = 20$

Figure 48: $\phi_s = 90$ [deg], $f = 600$ [MHz] - Far field pattern comparison for different values of w'.

2.3.4 Final Summary ($\phi_s = 90$ [deg], $f = 600$ [MHz])

$w' = 10.3$ [λ]				
	Virtual Array	**Physical Array**		
Environment	Free-Space	Free-Space (No-SI)	Aniso-Lens (SI)	Iso-Lens (SI)
Number of elements	16	15		
Spacing [λ]	0.5	0.5		
Aperture [λ]	7.5	7.0		
$D_{\max}$ [dB]	13.97	13.71	13.98	13.83
SLL [dB]	13.11	13.08	13.00	13.90
$FNBW$ [deg]	14.32	15.31	14.05	15.04
3dB Beamwidth [deg]	6.36	6.76	6.20	6.57
Matching Error, ξ (w.r.t. virtual, outside lens)	-	3.24×10^{-1}	4.30×10^{-1}	5.26×10^{-1}

$w' = 11.3$ [λ]				
	Virtual Array	**Physical Array**		
Environment	Free-Space	Free-Space (No-SI)	Aniso-Lens (SI)	Iso-Lens (SI)
Number of elements	17	15		
Spacing [λ]	0.5	0.5		
Aperture [λ]	8.0	7.0		
$D_{\max}$ [dB]	14.25	13.71	14.20	13.97
SLL [dB]	13.16	13.08	12.95	14.50
$FNBW$ [deg]	13.60	15.31	13.24	14.86
3dB Beamwidth [deg]	5.97	6.76	5.83	6.40
Matching Error, ξ (w.r.t. virtual, outside lens)	-	5.57×10^{-1}	5.69×10^{-1}	8.22×10^{-1}

$w' = 12.1$ [λ]				
	Virtual Array	**Physical Array**		
Environment	Free-Space	Free-Space (No-SI)	Aniso-Lens (SI)	Iso-Lens (SI)
Number of elements	18	15		
Spacing [λ]	0.5	0.5		
Aperture [λ]	8.5	7.0		
$D_{\max}$ [dB]	14.50	13.71	14.27	13.98
SLL [dB]	13.14	13.08	12.84	14.72
$FNBW$ [deg]	12.79	15.31	12.79	14.86
3dB Beamwidth [deg]	5.64	6.76	5.64	6.37
Matching Error, ξ (w.r.t. virtual, outside lens)	-	6.60×10^{-1}	5.38×10^{-1}	1.01

$w' = 12.9$ [λ]				
	Virtual Array	**Physical Array**		
Environment	Free-Space	Free-Space (No-SI)	Aniso-Lens (SI)	Iso-Lens (SI)
Number of elements	19	15		
Spacing [λ]	0.5	0.5		
Aperture [λ]	9.0	7.0		
$D_{\max}$ [dB]	14.73	13.71	14.26	13.94
SLL [dB]	13.06	13.08	12.78	14.99
$FNBW$ [deg]	12.07	15.31	12.43	15.22
3dB Beamwidth [deg]	5.35	6.76	5.52	6.45
Matching Error, ξ (w.r.t. virtual, outside lens)	-	6.46×10^{-1}	6.10×10^{-1}	1.27

$w' = 13.6$ [λ]				
	Virtual Array	**Physical Array**		
Environment	Free-Space	Free-Space (No-SI)	Aniso-Lens (SI)	Iso-Lens (SI)
Number of elements	20	15		
Spacing [λ]	0.5	0.5		
Aperture [λ]	9.5	7.0		
$D_{\max}$ [dB]	14.96	13.71	14.17	13.87
SLL [dB]	13.18	13.08	12.74	15.20
$FNBW$ [deg]	11.44	15.31	12.43	15.48
3dB Beamwidth [deg]	5.06	6.76	5.49	6.55
Matching Error, ξ (w.r.t. virtual, outside lens)	-	6.37×10^{-1}	6.97×10^{-1}	1.46

Table X: $\phi_s = 90$ [deg], $f = 600$ [MHz] - Final summary.

2.3.5 Final Summary: Performances vs. w' (vs. N')

Anisotropic Lens - $\phi_s = 90$ [deg]

This figure compares the pattern characteristics of

1. Original array ($N = 15$ elements, $d = \lambda/2$, Free-Space) - GREY;
2. Target array ($N' > N$ elements, $d = \lambda/2$, Free-Space) - RED;
3. QCTO-SI array ($N = 15$ elements, $d = \lambda/2$, Anisotropic Lens + SI) - CYAN;

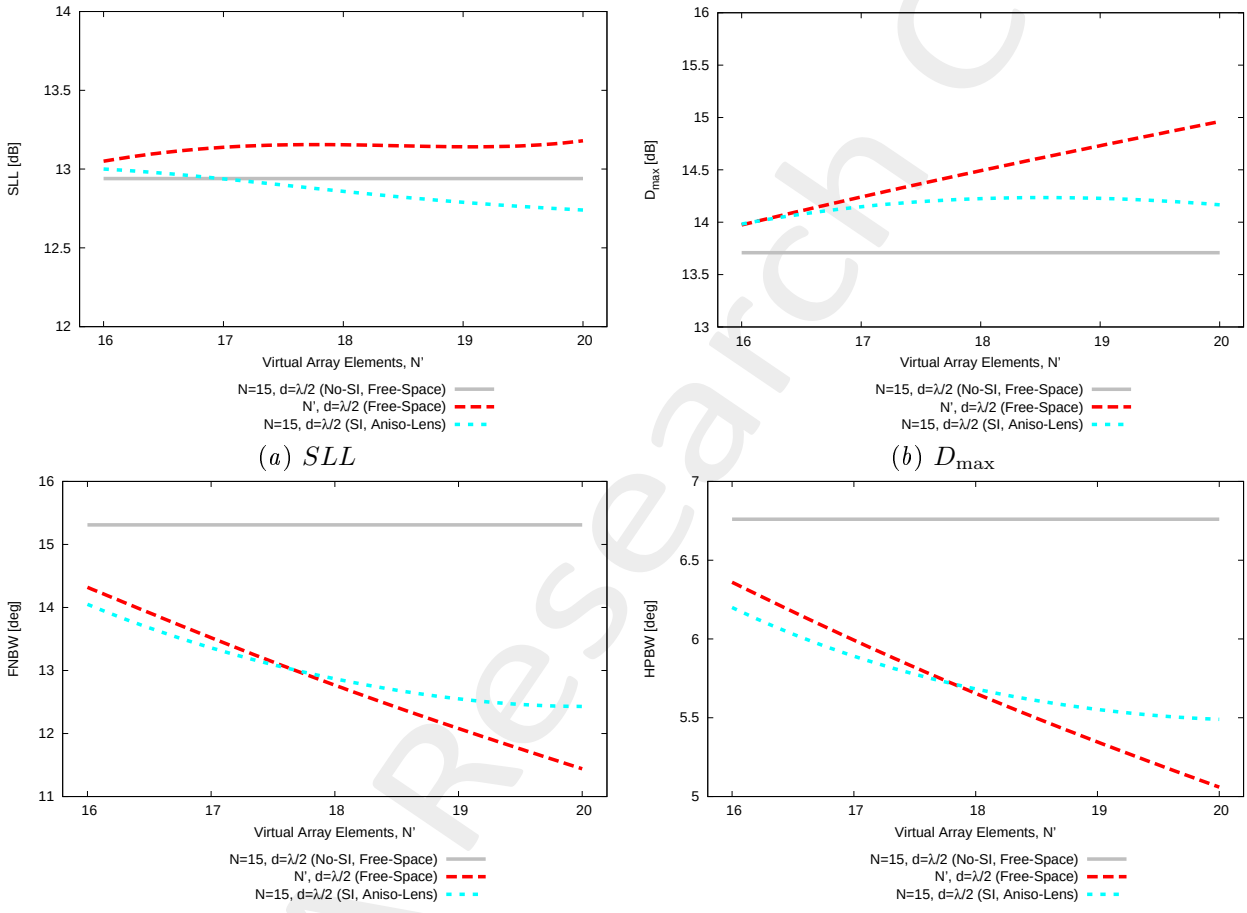

(a) SLL (b) $D_{\max}$

(b) $FNBW$ (c) $HPBW$

Figure 49: Aniso-Lens, $f = 600$ [MHz] - Pattern performances vs w' (vs. N').

3 Half-Cosine Profile - Comparisons

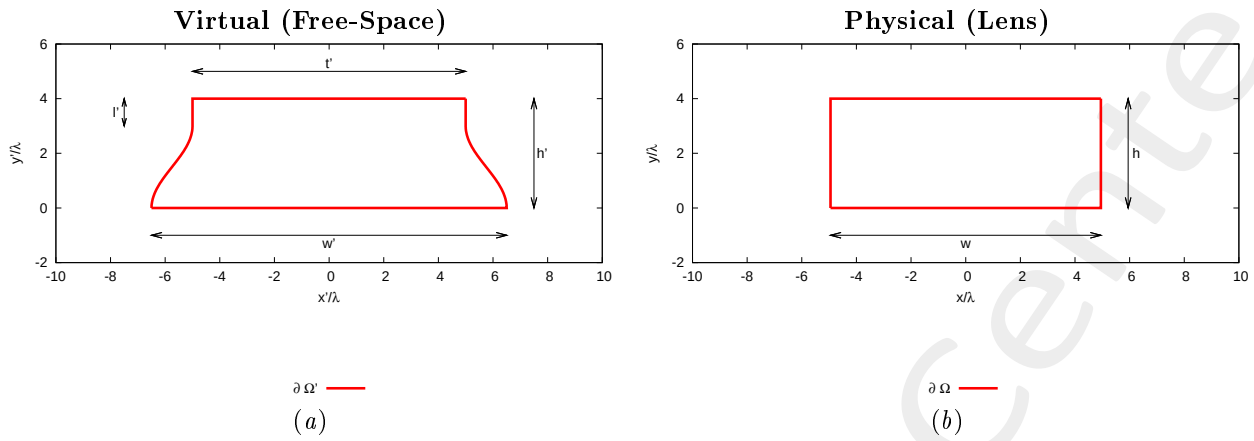

Figure 50: Transformation regions. The lower side of both virtual and physical boundaries are supposed to be PEC.

Analyzed configurations

1. $h' = 4.0$ [λ], $l' = 1.0$ [λ], $t' = 10.0$ [λ], $N = 15$;
2. $h' = 4.0$ [λ], $l' = 1.0$ [λ], $\mathbf{t' = 9.0}$ [λ], $N = 15$;
3. $h' = 4.0$ [λ], $l' = \mathbf{0.0}$ [λ], $t' = 9.0$ [λ], $N = 15$;

3.1 Far-Field Patterns ($\phi_s = 90$ [deg], $f = 600$ [MHz]), After SI, Anisotropic Lens

Case $N = 15 \rightarrow N' = 20$

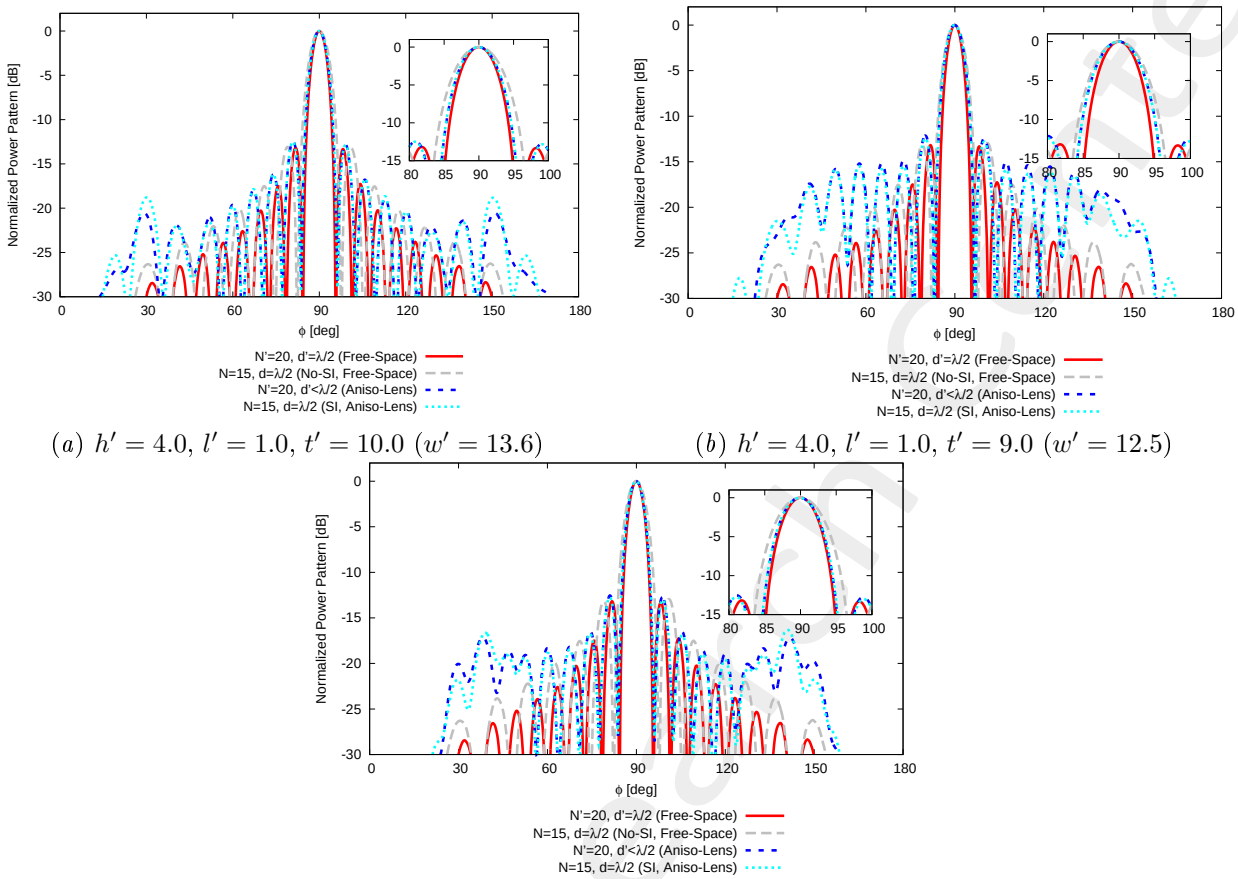

(a) $h' = 4.0$, $l' = 1.0$, $t' = 10.0$ ($w' = 13.6$)

(b) $h' = 4.0$, $l' = 1.0$, $t' = 9.0$ ($w' = 12.5$)

(c) $h' = 4.0$, $l' = 0.0$, $t' = 9.0$ ($w' = 13.6$)

Figure 51: $\phi_s = 90$ [deg], $f = 600$ [MHz] - Far field pattern comparison after SI step.

Observations

1. $h' = 4.0$ [λ], $l' = 1.0$ [λ], $\mathbf{t' = 10.0}$ [λ] $\rightarrow$ $h' = 4.0$ [λ], $l' = 1.0$ [λ], $\mathbf{t' = 9.0}$ [λ]
   - The reduction of t' leads to worse results, especially in terms of $FNBW$ and $HPBW$;
   - An increase of the side lobes is obtained;
2. $h' = 4.0$ [λ], $\mathbf{l' = 1.0}$ [λ], $t' = 9.0$ [λ] $\rightarrow$ $h' = 4.0$ [λ], $\mathbf{l' = 0.0}$ [λ], $t' = 9.0$ [λ]
   - The reduction of l' leads to better results;
   - $h' = 4.0$ [λ], $l' = 0.0$ [λ], $t' = 9.0$ [λ] seems to provide comparable results, in terms of $FNBW$ and $HPBW$, w.r.t. the case $h' = 4.0$ [λ], $l' = 1.0$ [λ], $t' = 0.0$ [λ]; however, external side-lobes seem slightly higher.

References

[1] G. Oliveri, G. Gottardi, F. Robol, A. Polo, L. Poli, M. Salucci, M. Chuan, C. Massagrande, P. Vinetti, M. Mattivi, R. Lombardi, and A. Massa, "Co-design of unconventional array architectures and antenna elements for 5G base station," *IEEE Trans. Antennas Propag.*, vol. 65, no. 12, pp. 6752-6767, Dec. 2017.

[2] P. Rocca, G. Oliveri, R. J. Mailloux, and A. Massa, "Unconventional phased array architectures and design methodologies - A review," *Proc. IEEE*, vol. 104, no. 3, pp. 544-560, Mar. 2016.

[3] G. Oliveri, M. Salucci, N. Anselmi and A. Massa, "Multiscale System-by-Design synthesis of printed WAIMs for waveguide array enhancement," *IEEE J. Multiscale Multiphysics Computat. Techn.*, vol. 2, pp. 84-96, 2017.

[4] A. Massa and G. Oliveri, "Metamaterial-by-Design: Theory, methods, and applications to communications and sensing - Editorial," *EPJ Applied Metamaterials*, vol. 3, no. E1, pp. 1-3, 2016.

[5] L. Poli, G. Oliveri, P. Rocca, M. Salucci, and A. Massa, "Long-Distance WPT Unconventional Arrays Synthesis," *J. Electromagnet. Wave.*, vol. 31, no. 14, pp. 1399-1420, Jul. 2017.

[6] G. Oliveri, F. Viani, N. Anselmi, and A. Massa, "Synthesis of multi-layer WAIM coatings for planar phased arrays within the system-by-design framework," *IEEE Trans. Antennas Propag.*, vol. 63, no. 6, pp. 2482-2496, Jun. 2015.

[7] G. Oliveri, L. Tenuti, E. Bekele, M. Carlin, and A. Massa, "An SbD-QCTO approach to the synthesis of isotropic metamaterial lenses," *IEEE Antennas Wireless Propag. Lett.*, vol. 13, pp. 1783-1786, 2014.

[8] G. Oliveri, D. H. Werner, and A. Massa, "Reconfigurable electromagnetics through metamaterials - A review" *Proc. IEEE*, vol. 103, no. 7, pp. 1034-1056, Jul. 2015.

[9] G. Oliveri, E. T. Bekele, M. Salucci, and A. Massa, "Transformation electromagnetics miniaturization of sectoral and conical horn antennas," *IEEE Trans. Antennas Propag.*, vol. 64, no. 4, pp. 1508-1513, Apr. 2016.

[10] G. Oliveri, E. T. Bekele, M. Salucci, and A. Massa, "Array miniaturization through QCTO-SI metamaterial radomes," *IEEE Trans. Antennas Propag.*, vol. 63, no. 8, pp. 3465-3476, Aug. 2015.

[11] G. Oliveri, E. T. Bekele, D. H. Werner, J. P. Turpin, and A. Massa, "Generalized QCTO for metamaterial-lens-coated conformal arrays," *IEEE Trans. Antennas Propag.*, vol. 62, no. 8, pp 4089-4095, Aug. 2014.

[12] G. Oliveri, E. Bekele, M. Carlin, L. Tenuti, J. Turpin, D. H. Werner, and A. Massa, "Extended QCTO for innovative antenna system designs," IEEE Antenna Conference on Antenna Measurements and Applications (CAMA 2014), pp. 1-3, Nov. 16-19, 2014.

[13] G. Oliveri, P. Rocca, M. Salucci, E. T. Bekele, D. H. Werner, and A. Massa, "Design and synthesis of innovative metamaterial-enhanced arrays," IEEE International Symposium on Antennas Propag. (APS/URSI 2013), Orlando, Florida, USA, pp. 972 - 973, Jul. 7-12, 2013.

[14] G. Oliveri, "Improving the reliability of frequency domain simulators in the presence of homogeneous metamaterials - A preliminary numerical assessment," *Progress In Electromagnetics Research*, vol. 122, pp. 497-518, 2012.

[15] M. Salucci, G. Oliveri, N. Anselmi, G. Gottardi, and A. Massa, "Performance enhancement of linear active electronically-scanned arrays by means of MbD-synthesized metalenses," *J. Electromagnet. Wave.*, vol. 0, no. 0, pp. 1-29, 2017 (DOI: 10.1080/09205071.2017.1410077).